

## ABSTRACT

OUYANG, JING. Piezoresistive Self-Sensing and Feedback Control of a Z-Shaped Thermal Actuator. (Under the direction of Dr. Yong Zhu).

This thesis demonstrates the feasibility of self-sensing of a Z-shaped thermal actuator (ZTA). Based upon this characteristic, a feedback system is developed to hold the position of the ZTA. The Z-shaped actuator is modeled analytically for obtaining its displacement, stiffness, stability and output force. Multiphysics finite element analysis for ZTA static response is performed and verified by the experimental measurements. In addition, the dynamic performances of ZTA were analyzed and measured. Moreover an *in-situ* SEM nanomanipulation process is used to characterize the piezoresistive response of ZTAs, which shows that ZTAs can be used as piezoresistive sensors for sensing the external force and displacement. The experimental results agree very well with multiphysics simulations for piezoresistive effect experiment. A new feedback scheme is further explored, where the ZTA is treated as a two-input (applied current and external force) and two-output (displacement and electric resistance) system. Based on the calibrated relationships between the inputs and the outputs, a feedback system is developed, which can simultaneously sense the external force and generate updated current to actuate the ZTA to the desired position. We demonstrate the performance of this feedback control by holding the ZTA at a constant position under various external forces.

© Copyright 2011 by Jing Ouyang

All Rights Reserved

Piezoresistive Self-Sensing and Feedback Control of a Z-Shaped Thermal Actuator

by  
Jing Ouyang

A thesis submitted to the Graduate Faculty of  
North Carolina State University  
in partial fulfillment of the  
requirements for the degree of  
Master of Science

Mechanical Engineering

Raleigh, North Carolina

2011

APPROVED BY:

---

Dr. Yong Zhu  
Committee Chair

---

Dr. Fen Wu

---

Dr. Jingyan Dong

**DEDICATION**

*To My Beloved Parents!*

## **BIOGRAPHY**

Jing Ouyang was born in Changsha, China on May 31<sup>st</sup>, 1986, and graduated in 2005 from Changsha First High School, China. He entered Center South University that autumn in the department of Mechanical and Electrical Engineering majoring Microelectronics Manufacture and graduated in 2009. In 2010 spring, he enrolled in the department of Mechanical and Aerospace Engineering at North Carolina State University in Raleigh. His work is focusing on Microelctromechnical Systems (MEMS) design and testing and feedback control system.

## ACKNOWLEDGMENTS

First and foremost, I would like to thank my advisor, Dr. Yong Zhu, for his patience, guidance, and encouragement throughout my entire time at NC State. It is him introducing me into the MEMS field. It is him sharing his experience of doing research and living in US. It is him enlightening me a lot. Thank you!

I also would like to thank my other two thesis committee members, Professor Fen Wu and Professor Jingyan Dong for their reviewing the manuscript and advice, and taking the time to be on my advisory committee. And special thank to Professor Jingyan Dong for valuable discussion on the feedback control. Thank you!

I would like to express my appreciation to my colleagues in my lab, Feng Xu, John W. Durham III and Qingquan Qin. Thanks Qingquan Qin for his helping perform the *in-situ* SEM experiments. Thanks John for discussions on the ANSYS simulation. Thank you!

I would also like to give my appreciation to Analytical Instrumentation Facility at North Carolina State University for providing the SEM which facilitated this work. Thank you!

Last but not the least, to my family and close friends, especially my girlfriend, Daisha Cai, I am grateful for your support, encouragement and understanding through the ups and downs of life experienced in graduate school. Thank you!

This research was funded by National Science Foundation.

## TABLE OF CONTENTS

<b>LIST OF TABLES .....</b>	<b>vii</b>
<b>LIST OF FIGURES .....</b>	<b>viii</b>
<b>Chapter 1 Introduction .....</b>	<b>1</b>
1.1 Actuators and Sensors.....	2
1.1.1 Actuators .....	2
1.1.2 Sensors .....	6
1.2 Piezoresistive Effect on Single Crystalline Silicon (SCS).....	9
1.3 Our Approach.....	11
<b>Chapter 2 Z-Shaped Thermal Actuator (ZTA) Description.....</b>	<b>12</b>
2.1 Mechanism.....	12
2.2 SOIMUMPs Process .....	15
2.3 Static Response .....	17
2.3.1. Multiphysics Simulation .....	17
2.3.2. Experimental Results .....	24
2.4 Dynamic Response.....	25
<b>Chapter 3 Piezoresistive Effect Experiment.....</b>	<b>29</b>
3.1 Piezoresistive self-sensing of the ZTA .....	29
3.1.1 Experimental Measurement of Piezoresistivity .....	29
3.1.2 Experimental Results of Piezoresistivity .....	31
3.2 Multiphysics FEA .....	35
<b>Chapter 4 Feedback Control of the ZTA.....</b>	<b>37</b>
4.1 Data Fitting of the Piezoresistivity Measurements .....	37
4.2 Design of Feedback Control System.....	42
4.3 Experimental Results of Feedback Control .....	44
<b>Chapter 5 Conclusion .....</b>	<b>48</b>
5.1 Future Work .....	49
<b>REFERENCES.....</b>	<b>50</b>

<b>APPENDICES .....</b>	<b>55</b>
Appendix A.....	56

**LIST OF TABLES**

<b>Table 2.1</b> Dimensions of the Z-shaped thermal actuator used in simulations.....	18
<b>Table 2.2</b> Material parameters used in simulations.....	18
<b>Table 4.1</b> The comparison of original current and updated current under different external force applied for feedback experiment .....	46

## LIST OF FIGURES

<b>Figure 1.1</b> SEM image of comb drive.....	3
<b>Figure 1.2</b> Schematic of the V-shaped thermal actuator .....	4
<b>Figure 1.3</b> Schematic of U-shaped thermal actuator.....	4
<b>Figure 1.4</b> SEM picture of piezoelectric actuator .....	5
<b>Figure 1.5</b> Electrostatic sensor used in <i>in situ</i> nanowire tensile testing system.....	6
<b>Figure 1.6</b> (a) The top view of the zirconate titanate (PZT) chip. (b) The cross-sectional view and of the PZT chip arrangement.....	8
<b>Figure 2.1</b> SEM image of a Z-shaped thermal actuator. The black area is the etched hole underneath the actuator .....	12
<b>Figure 2.2</b> Free body diagram of single ZTA beam.....	13
<b>Figure 2.3</b> SOIMUMPs fabrication highlighted processing features.....	16
<b>Figure 2.4</b> Simulation results at 8.5 mA. (a) The displacement distribution of ZTA at the 8.5 mA current level. The unit is in micro-meter. (b) The temperature distribution of ZTA at the 8.5 mA current level. The unit is in Kelvin. (c) The voltage distribution of ZTA at the 8.5 mA current level. The unit is in Volt. ....	20
<b>Figure 2.5</b> The multiphysics simulation results. (a) The displacement simulation results. (b) The shuttle temperature simulation results. (c) The resistance (converted by output voltage results) simulation results. ....	22
<b>Figure 2.6</b> The experimentally static response of the ZTA comparing with simulated results (a) Displacement as functions of applied current. (b) Resistance as functions of applied current. ....	23
<b>Figure 2.7</b> Cross section of the actuator for thermal analysis .....	26
<b>Figure 2.8</b> Dynamic response of the ZTA. (a) Magnitude versus frequency. (b) Phase versus frequency.....	28
<b>Figure 3.1</b> The experimental process for the piezoresistivity measurement. (a) The gap between the ZTA and the manipulator probe tip is less than $D_1$ (581 nm at $I_1 = 8.6$ mA) to	

block the ZTA movement. (b) The probe pushes the ZTA back by 117 nm after $I_1$ is applied again to the ZTA .....	30
<b>Figure 3.2</b> (a) Voltage versus external force for all current levels. For each current, the external force starts as zero (no applied force) and increases. (b) Voltage versus displacement for all current levels .....	32
<b>Figure 3.3</b> The external force sensitivity at different current levels .....	33
<b>Figure 3.4</b> Noise of the resistance at the applied current of 8.6 mA. The red line is the average value of all the data points .....	34
<b>Figure 3.5</b> The simulation results at the 8.6 mA current level with the external force of 20 $\mu\text{N}$ . (a) Displacement of the shuttle changes from 0.584 $\mu\text{m}$ to 0.513 $\mu\text{m}$ . (b) Output voltage changes from 4.114 V to 4.109 V .....	35
<b>Figure 3.6</b> The comparison between the simulated and experimental results at 8.6, 8.8 and 9.0 mA current levels. In the multiphysics simulations, temperature-dependent resistivity and thermal expansion coefficient were used (see table 2). .....	36
<b>Figure 4.1</b> (a) The displacement and (b) the resistance change with the external force increasing at different current levels .....	38
<b>Figure 4.2</b> Data fitting for (a) displacement and (b) resistance using the piezoresistive experimental results .....	39
<b>Figure 4.3</b> (a) Displacement as a function of the applied current and external force. (b) Resistance as a function of the applied current and external force. ....	41
<b>Figure 4.4</b> Feedback control system with compensator block diagram .....	42
<b>Figure 4.5</b> Circuit diagram for converting the voltage signal to current signal. $V_R$ is the voltage on the dummy resistor (1 k $\Omega$ ), which is in series with the ZTA. With the measured current ( $=V_R / 1 \text{ k}\Omega$ ), the resistance of the ZTA is known by measuring $V_Z$ . $V_{\text{out}}$ was the voltage output from the data acquisition module (and the LabVIEW program) .....	43
<b>Figure 4.6</b> Overview of the closed-loop feedback experiment. The AFM cantilever is oriented perpendicular to the ZTA and parallel to the electron beam. The AFM tip is used to push the ZTA. (a) A schematic showing the position of the ZTA and cantilever. Left is side view and right is top view. $11^\circ$ tilt of the AFM cantilever is used to ensure a clear	

observation of the setup. (b) SEM image showing the overview of the closed-loop feedback setup. ....	44
<b>Figure 4.7</b> The feedback control experiment to maintain a constant position of the ZTA. Ideally $D_C$ equals $D_1$ . ....	45
<b>Figure 4.8</b> The error of the feedback control system .....	47
<b>Figure A-1</b> The layout drawing of SOIMUMPs 10mm × 10mm chip. The arrows show the Wheatstone bridge of Z-shaped thermal actuator .....	56

# Chapter 1 Introduction

In the field of microelectromechanical systems (MEMS), thermal actuators have emerged as compact, stable and high-force actuation apparatuses [1-4]. And they have been employed in a broad range of applications for obtaining in-plan displacement including on-chip nanoscale material testing system [5-7], linear and rotary microengine [8], nanopositioner [9], and bistable mechanism [10].

The project presented in this thesis is mainly focusing on that the Z-shaped thermal actuator (ZTA) treated as displacement sensor by its piezoresistive effect so that it is able to simultaneously sensing and actuating. Moreover, a closed-loop system is developed based on this sensing characteristic to hold the ZTA at a constant position under various external forces.

In Chapter 1, it firstly gives brief introduction of several popular actuators and sensors used in the area of MEMS. Piezoresistive effect is then described.

The device used in this project, ZTA, is specifically analyzed in Chapter 2. The mechanism of the device is shown firstly. Based on energy method, the static response is then analyzed, including displacement, stiffness, average temperature change on the device, etc. Experiments are carried out for attaining the static response and dynamic response of the ZTA. What's more, multiphysics simulation is performed in ANSYS 11.0 for comparison. The simulated results are coincident with the experimental results very well.

Piezoresistive response of our ZTA is demonstrated experimentally in Chapter 3. From the experimental results, it shows when the ZTA is experiencing external force, the resistance would linearly decrease. The rate of decreasing is related to the applied current. Therefore, it demonstrates that the ZTA could be as a piezoresistive sensor to sense the external force. A multiphysics simulation is also performed in ANSYS 11.0 for piezoresistive effect. As a result, the experimental results agree very well with multiphysics simulations.

In Chapter 4, based on the feature of the ZTA obtained in Chapter 3, a feedback controller is developed in LabVIEW 8.5 to hold the position of the ZTA under various external forces by applying extra compensation current.

In the final Chapter, conclusions and discussions are formed about the experiments we have done. We then outline the possible future research direction based on the feedback system we developed.

## **1.1 Actuators and Sensors**

Actuators and sensors are the major parts in MEMS. With the maturing of the MEMS, various actuators and sensors are designed and fabricated. For actuators, based on their actuating principles, they could be classified as electrostatic actuators, electrothermal actuators, piezoelectric actuators, and so forth. For sensors, the same as actuators are classified by their sensing principles, such as electrostatic sensors, piezoelectric sensors, piezoresistive sensors, etc. Different kind actuators and sensors have different features and functions. This part introduces several popular actuators and sensors used in MEMS area.

### **1.1.1 Actuators**

#### **Electrostatic Actuators**

Comb drive actuator (Figure1.1) is a typical electrostatic actuator which was demonstrated by Tang, *et al* in 1990 for the first time [11]. From then on, it has been used as actuator in many MEMS applications to generate the electrostatic force and displacement. Comb drive usually has two sets of interdigitated comb fingers – fixed set (stator) which is connected to the substrate [12], and movable set (rotor) which is connected to the compliant suspension. When a voltage difference is applied between the fixed and the movable sets, it will lead to a displacement of the movable set towards the fixed set by electrostatic forces generated between them. Depend upon the movement direction, commonly encountered linear comb drive actuator can be classified to three types: lateral [13;14] (or longitudinal [15]) vertical [16;17], and transverse [18].

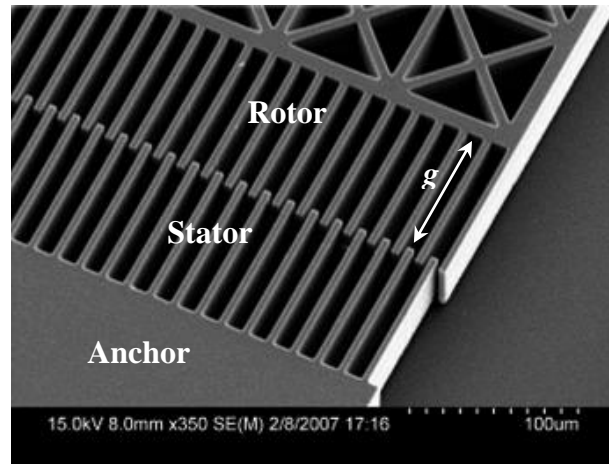


Figure 1.1 SEM Image of Comb Drive [14].

The advantages of electrostatic actuators are simplicity, low power consumption and fast response. However, there are several drawbacks of comb drive. Firstly, high actuation voltage is required. Secondly, to obtain relatively large force generated, much more combs needed resulting in more area occupied. Finally, pull-in effect would happen when the applied voltage is higher than  $\sqrt{\frac{8kg^3}{27A\epsilon}}$ , where  $k$  is the stiffness of the comb drive,  $g$  is the initial distance between movable and stable comb (as shown in Fig 1.1),  $A$  is the overlapped area of movable fingers and fixed fingers,  $\epsilon$  is the permittivity of vacuum which is a constant equaling  $8.85 \times 10^{-12} \text{ C}^2 / (\text{Nm}^2)$ . If pull-in effect happens, the device cannot be used anymore.

#### **Electro Thermal Actuator:**

There are two types of electro thermal actuators popularly used in MEMS area, namely V-shaped thermal actuator and U-shaped thermal actuator. The thermal actuators are basically depending upon the thermal expansion effect of the materials.

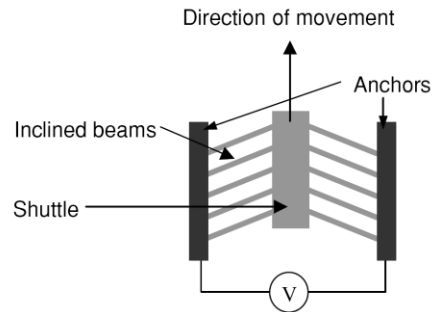


Figure 1.2 Schematic of the V-Shaped Thermal Actuator [5]

V-shaped thermal actuator, as shown in Figure 1.2, is consisted of several pairs of inclined beams which connected anchors and central free standing shuttle. After applying voltage difference to the both ends of the anchors, the current would pass through the whole actuator. Heat is accordingly generated in the whole body of the actuator due to Joule Heating [19]. And because of the thermal expansion effect, the raising temperature expands the beams, which pushes the shuttle to the direction shown in the Figure 1.2.

The stiffness of the V-shaped thermal actuators is relatively high comparing with other actuators so that they could generate high force.

U-shaped thermal actuator is based upon the asymmetrical thermal expansion of the two arms with made of the same conductive material [20]. The U-shaped thermal actuator is consisted of two arms with the same length, but different width (Figure 1.3). Since the resistance can be expressed as

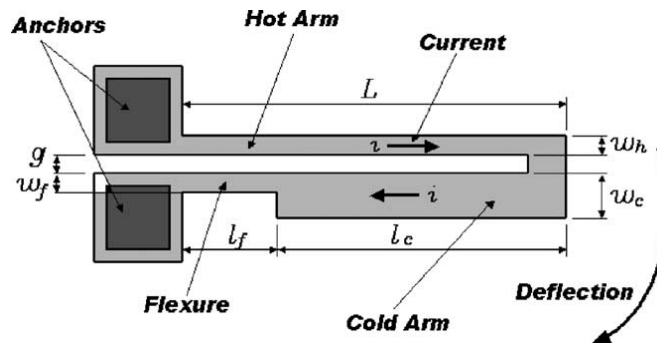


Figure 1.3 Schematic of U-Shaped Thermal Actuator [20]

$$R = \rho \frac{L}{A} \quad (1.1)$$

where  $\rho$  is the resistivity of the material;  $L$  and  $A$  are the length and cross sectional area of the resistor, respectively. Because the cross sectional shape is rectangle, the area is the product of the width times the thickness of the thermal actuator. Therefore, the resistance of the arm is in inverse proportion to the width. According to the Equation 1.2, the smaller the resistance is, the higher the temperature can be reached when applying the same voltage.

$$H = P = \frac{V^2}{R} \quad (1.2)$$

where  $H$  is the heat generated by resistor;  $P$  is the power; and  $V$  is the voltage applied to the resistor. Therefore, the rising temperature  $\Delta T$  of narrower arm (hot arm in Figure 1.3) of the thermal actuator is higher than the wider arm (cold arm in Figure 1.3) due to its smaller width. Since the length change is proportional to the temperature change (Equation 1.3), the length of hot arm can be extended more than cold arm, so that the actuator is able to bend to the cold arm side to obtain the deflection.

$$\frac{\Delta L}{L} = \alpha \Delta T \quad (1.3)$$

### Piezoelectric Actuator

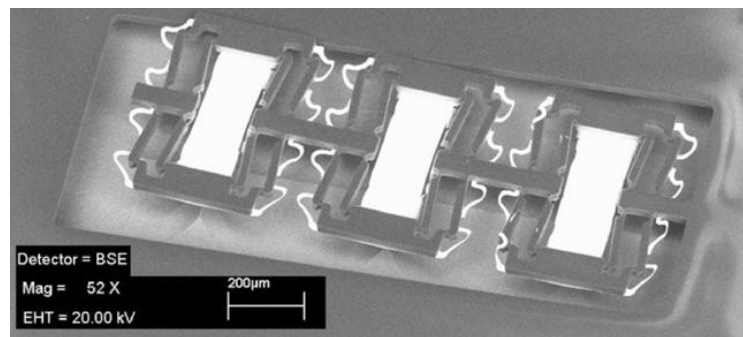


Figure 1.4 SEM picture of piezoelectric actuator. [21]

Piezoelectric actuator is based on the piezoelectric effect. When the electric field is applied to the actuator, the deflection is produced. And the relationship between the electric field and deflection of the piezoelectric materials is given by the following equation [15]:

$$\begin{bmatrix} s_1 \\ s_2 \\ s_3 \\ s_4 \\ s_5 \\ s_6 \end{bmatrix} = \begin{bmatrix} S_{11} & S_{12} & S_{13} & S_{14} & S_{15} & S_{16} \\ S_{21} & S_{22} & S_{23} & S_{24} & S_{25} & S_{26} \\ S_{31} & S_{32} & S_{33} & S_{34} & S_{35} & S_{36} \\ S_{41} & S_{42} & S_{43} & S_{44} & S_{45} & S_{46} \\ S_{51} & S_{52} & S_{53} & S_{54} & S_{55} & S_{56} \\ S_{61} & S_{62} & S_{63} & S_{64} & S_{65} & S_{66} \end{bmatrix} \begin{bmatrix} T_1 \\ T_2 \\ T_3 \\ T_4 \\ T_5 \\ T_6 \end{bmatrix} + \begin{pmatrix} d_{11} & d_{21} & d_{31} \\ d_{12} & d_{22} & d_{32} \\ d_{13} & d_{23} & d_{33} \\ d_{14} & d_{24} & d_{34} \\ d_{15} & d_{25} & d_{35} \\ d_{16} & d_{26} & d_{36} \end{pmatrix} \begin{bmatrix} E_1 \\ E_2 \\ E_3 \end{bmatrix} \quad (1.4)$$

where the  $[s]$  is the strain vector.  $[S]$  is the compliance matrix. The terms  $T_1$  through  $T_3$  are the normal stresses along axes X, Y, and Z, while  $T_4$  through  $T_6$  are shear stresses.  $(d)$  is the piezoelectric constant matrix.  $[E]$  is the electrical field vector. And the Equation 1.4 can be simplified as following format,

$$s = ST + dE \quad (1.5)$$

If no mechanical stress applied, the strain would only be related to the electric field, and the first term on the right-hand side of Equation 1.5 can be eliminated.

## 1.1.2 Sensors

### Electrostatic sensors

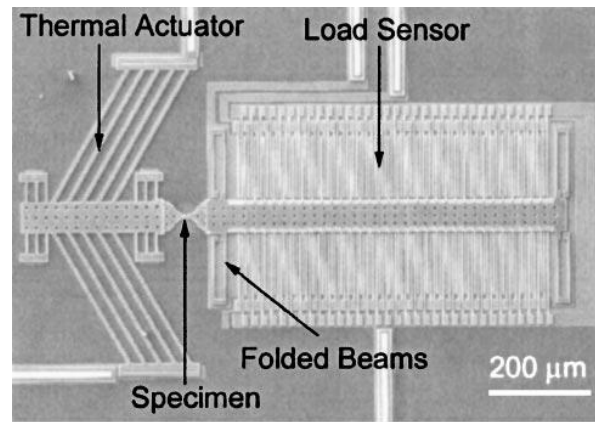


Figure 1.5 Electrostatic sensor used in *in situ* nanowire tensile testing system [7].

Parallel plate capacitive sensors are the most fundamental electrostatic sensors used in MEMS (shown in Figure 1.4). As its name suggests, it consists of two conducting plates with their broad sides parallel to each other. Since the capacitance of a parallel-plate capacitor is

$$C \equiv \frac{Q}{V} = \frac{Q}{Ed} = \frac{Q}{\frac{Q}{\varepsilon A}d} = \frac{\varepsilon A}{d} \quad (1.6)$$

where  $Q$  is the amount of stored charge,  $V$  is the applied voltage,  $E$  is the primary electric field,  $\varepsilon$  is the permittivity of the media,  $A$  is the overlapping area and  $d$  is the spacing between two plates. It is obvious that the capacitance of a parallel-plate capacitor is proportional to the overlapping area, inversely proportional to the spacing. Therefore, the sensors are able to detect the displacement along two directions, normal displacement (spacing will change) or parallel-sliding displacement (overlapped area will change), by detecting the entire capacitor change. In the meantime, based on its stiffness, external force can also be obtained by  $F=k \times U$ , where  $k$  is the stiffness of the sensor, and  $U$  is the displacement.

However, the limitations of the electrostatic sensors are as following description. Firstly relatively large space occupied. Secondly, the detection of position is constrained to small vertical movement or horizontal movement. Finally, the output signal is small and easily be influenced by noise.

### **Piezoelectric Sensor**

Recently, piezoelectric sensor has been integrated into MEMS technology. Piezoelectric sensor is based upon the direct effect of piezoelectricity, which is when the piezoelectric materials are under mechanical stress, they can generate an electric voltage. The general constitutive equation can be expressed as

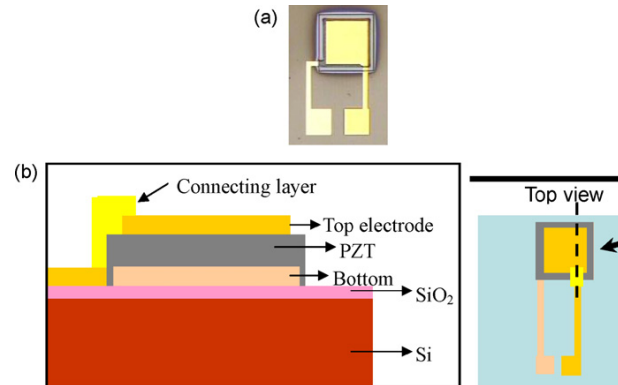


Figure 1.6 (a) The top view of the zirconate titanate (PZT) chip. (b) The cross-sectional view and of the PZT chip arrangement. [22]

$$\begin{bmatrix} D_1 \\ D_2 \\ D_3 \end{bmatrix} = \begin{bmatrix} d_{11} & d_{12} & d_{13} & d_{14} & d_{15} & d_{16} \\ d_{21} & d_{22} & d_{23} & d_{24} & d_{25} & d_{26} \\ d_{31} & d_{32} & d_{33} & d_{34} & d_{35} & d_{36} \end{bmatrix} \begin{bmatrix} T_1 \\ T_2 \\ T_3 \\ T_4 \\ T_5 \\ T_6 \end{bmatrix} + \begin{pmatrix} \epsilon_{11} & \epsilon_{12} & \epsilon_{13} \\ \epsilon_{21} & \epsilon_{22} & \epsilon_{23} \\ \epsilon_{31} & \epsilon_{32} & \epsilon_{33} \end{pmatrix} \begin{bmatrix} E_1 \\ E_2 \\ E_3 \end{bmatrix} \quad (1.7)$$

where  $[D]$  represents the electrical polarization,  $[d]$  represents the piezoelectric constant matrix,  $(\epsilon)$  represents the permittivity matrix. Equation 1.7 can be simplified as

$$D = dT + \epsilon E \quad (1.8)$$

If no electric field is involved, the second term on the right-hand side of Equation 1.8 could be eliminated. Therefore, the external force could be attained due to the relationship between the voltage change and the external stress. Zirconate titanate (PZT) is the most popular piezoelectric sensor material (shown in Figure 1.6).

### Piezoresistive sensors

Piezoresistive sensors are more like piezoelectric sensors. However, piezoresistive sensors are based on piezoresistive effect, i.e. the resistivity of the sensor will change when external stress is applied resulting in the output signal (voltage or current) change. Therefore, the external force could be calculated. The details of piezoresistive effect on single crystalline silicon would be presented in the following part.

## 1.2 Piezoresistive Effect on Single Crystalline Silicon (SCS)

The piezoresistive effect is a widely used sensing principle since it was documented by C. Smith in 1954 [23]. When a piezoresistive material is experiencing a strain, its resistivity may change. Depending on it, the mechanical change, which is difficult to be detected, could be obtained via capturing the electrical signal change. Today, the piezoresistive effect has been widely used in the MEMS field for sensing applications, such as cantilever sensors [24-26], pressure sensors [27;28], strain gauges [29], accelerometers [30;31], shear stress sensors [32;33], gyro rotation rate sensors [34;35], tactile sensors [36;37], and flow sensors [38].

The electric resistance ( $R$ ) of a structure is a function of its dimensions and resistivity ( $\rho$ ) as shown in Equation 1.1. When the resistor is experiencing external force, the relative change in resistance could be calculated by [39]

$$\frac{\Delta R}{R} = \frac{\Delta l}{l} - \frac{\Delta w}{w} - \frac{\Delta t}{t} + \frac{\Delta \rho}{\rho} \quad (1.9)$$

Since the width, thickness and length of a structure are related to Poisson effect, and the relation could be expressed as

$$\frac{\Delta w}{w} = \frac{\Delta t}{t} = -\nu \frac{\Delta l}{l} \quad (1.10)$$

where  $\nu$  is Poisson's ratio of the material. Consequently, Equation 1.9 could be simplified as

$$\frac{\Delta R}{R} = (1 + 2\nu)\varepsilon + \frac{\Delta \rho}{\rho} \quad (1.11)$$

where  $\varepsilon$  is the strain ( $\frac{\Delta l}{l}$ ). From this equation, it is known that the electric resistance change is due to two factors: dimensional change which is dominated by the first and second term in Equation 1.11, and resistivity change which is dominated by the last term. In semiconductor gauges, as Y. Kanda mentioned in [39], the resistivity change is approximately 50 times larger than the dimensional change. Therefore, the resistivity change is dominant. And piezoresistive effect is the very effect that changes the resistance by changing the resistivity when experienced external force. Moreover, gauge factor ( $GF$ ) is

introduced to represent the ratio of relative change in electrical resistance to the mechanical strain

$$GF = \frac{\Delta R}{R} / \varepsilon = 1 + 2\nu + \frac{\Delta \rho}{\rho} / \varepsilon \quad (1.12)$$

Because the piezoresistive coefficients ( $\pi$ ) relate to two second-rank tensors of stress and resistivity, they require four subscripts to be expressed completely. The first and second subscripts relate to resistivity as measured electric field potential and the current density, respectively; the third and fourth subscripts represent the stress. For the purpose of conciseness, the subscripts of each tensor are collapsed, for instance,  $\pi_{1111}$  is simplified to  $\pi_{11}$ ,  $\pi_{1122}$  to  $\pi_{12}$ ,  $\pi_{2323}$  to  $\pi_{44}$ . The piezoresistive tensor could be fully characterized as a matrix,

$$[\pi] = \begin{bmatrix} \pi_{11} & \pi_{12} & \pi_{13} & \pi_{14} & \pi_{15} & \pi_{16} \\ \pi_{21} & \pi_{22} & \pi_{23} & \pi_{24} & \pi_{25} & \pi_{26} \\ \pi_{31} & \pi_{32} & \pi_{33} & \pi_{34} & \pi_{35} & \pi_{36} \\ \pi_{41} & \pi_{42} & \pi_{43} & \pi_{44} & \pi_{45} & \pi_{46} \\ \pi_{51} & \pi_{52} & \pi_{53} & \pi_{54} & \pi_{55} & \pi_{56} \\ \pi_{61} & \pi_{62} & \pi_{63} & \pi_{64} & \pi_{65} & \pi_{66} \end{bmatrix} \quad (1.13)$$

However, for semiconductor material, there are only three independent coefficients, namely  $\pi_{11}$ ,  $\pi_{12}$  and  $\pi_{44}$ . Therefore, the matrix could be simplified as

$$[\pi] = \begin{bmatrix} \pi_{11} & \pi_{12} & \pi_{13} & 0 & 0 & 0 \\ \pi_{21} & \pi_{22} & \pi_{23} & 0 & 0 & 0 \\ \pi_{31} & \pi_{32} & \pi_{33} & 0 & 0 & 0 \\ 0 & 0 & 0 & \pi_{44} & 0 & 0 \\ 0 & 0 & 0 & 0 & \pi_{44} & 0 \\ 0 & 0 & 0 & 0 & 0 & \pi_{44} \end{bmatrix} \quad (1.14)$$

Mason and Thurston used bonded gauges with longitudinal orientations to measure displacement, force, and torque [40]. They also presented more general formulations for longitudinal ( $\pi_l$ ) and transverse ( $\pi_t$ ) piezoresistive coefficients for a gauge in an arbitrary crystal direction as

$$\pi_l = \pi_{11} - 2(\pi_{11} - \pi_{12} - \pi_{44}) \times (l_1^2 m_1^2 + l_1^2 n_1^2 + n_1^2 m_1^2) \quad (1.15a)$$

$$\pi_t = \pi_{12} + 2(\pi_{11} - \pi_{12} - \pi_{44}) \times (l_1^2 l_2^2 + m_1^2 m_2^2 + n_1^2 n_2^2) \quad (1.15b)$$

where  $l$ ,  $m$  and  $n$  are the direction cosines of the direction associated with  $(\pi_l)$  and  $(\pi_t)$ , with respect to the crystallographic axes.

The N- type piezoresistors exhibit opposite trends to the P- type piezoresistors in resistance change and different direction-dependent magnitudes under stress. The magnitude and sign of the piezoresistive coefficients ( $\pi$ ) depend upon several factors including impurity concentration, temperature, crystallographic direction, as well as the relation of voltage, current and stress to one another [41].

### **1.3 Our Approach**

The ZTA static responses in vacuum environment were tested and simulated. The dynamic response of this device was analyzed and tested. The piezoresistive effect on the ZTA was then tested by using the manipulate tip to apply the external force to push the ZTA back, meanwhile obtaining the output signal change to calculate the electric resistance change with the external force. We fitted the relation between two inputs, i.e. current and external force, and two outputs, displacement and resistance. Then based on these fitting equations, we developed a feedback system to hold the position of the ZTA in LabVIEW 8.5. We tested the feasibility of the feedback system under ranging from 6 to 9.5 mA current levels with different external forces.

## Chapter 2 Z-Shaped Thermal Actuator (ZTA)

### Description

#### 2.1 Mechanism

The Z-Shaped electro-thermal actuator, designed by C. Guan and Y. Zhu [2], consists of two pairs of beams symmetrically connected to a central shuttle. The ends of the beams are anchored to the substrate to fix the movement and rotation, as well as to provide the electric connection and transportation.

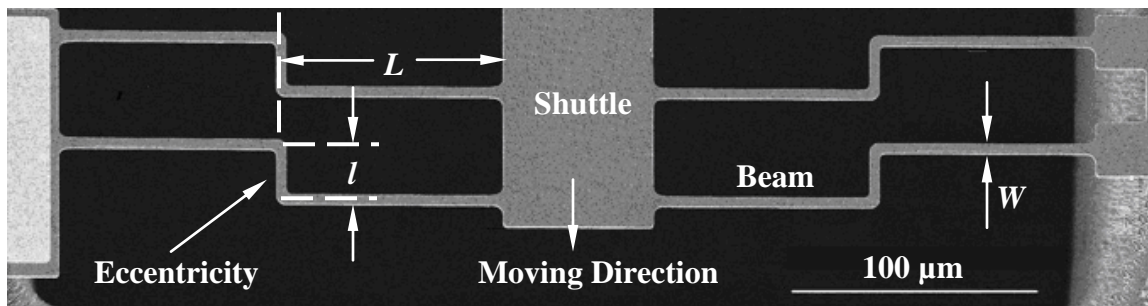


Figure 2.1 SEM image of a Z-shaped thermal actuator. The black area is the etched hole underneath the actuator.

The mechanics of this Z-Shaped electro-thermal actuator are, as shown in the Figure 2.1, that after applying the input voltage across the beams, the Joule Heating effect generates heat and temperature rise along the beams. As a result, thermal expansion happens within the beams. Due to the short vertical beam in the Z-shape design (eccentricity as defined in Figure 2.1) and the overall symmetry, the Z-shaped beam deflects towards the desired direction and hence forces the central shuttle forward [2].

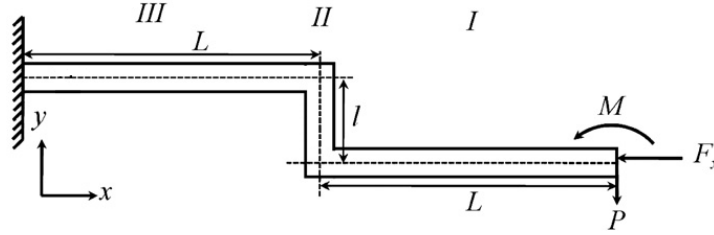


Figure 2.2 Free body diagram of single ZTA beam [2].

The mechanical response of the ZTA structure is able to be computed by using energy method. Based on its symmetric structure, we can analyze one beam of the ZTA to derive the stiffness, displacement, temperature and internal force as functions of the device's dimensions. The free body diagram is given in Figure 2.2. Three reaction loads, shown in Figure 2.2, are considered: 1) the axial force,  $F_x$ ; 2) the moment,  $M$ ; and 3) the virtual force  $P$  (in order to gain the displacement). During calculation, we set  $P$  equal to 0. The moment in the three segments (shown in Figure 2.2 as  $I$ ,  $II$ , and  $III$ ) is

$$\begin{cases} M_1(x_1) = Px_1 - M & 0 < x_1 < L \\ M_2(x_2) = PL - M + x_2 F_x & 0 < x_2 < l \\ M_3(x_3) = P(L + x_3) - M + l F_x & 0 < x_3 < L \end{cases} \quad (2.1)$$

By using strain energy method [42], the displacement and rotation could be obtained

$$\begin{cases} D_x = 2\alpha\Delta TL = 2 \int_0^L \frac{F_x}{EA} dx + \int_0^L \frac{M_1(x)}{EI} \frac{\partial M_1}{\partial F_x} dx + \int_0^L \frac{M_2(x)}{EI} \frac{\partial M_2}{\partial F_x} dx + \int_0^L \frac{M_3(x)}{EI} \frac{\partial M_3}{\partial F_x} dx \\ \quad = \left(\frac{2L}{EA} + \frac{l^3}{3EI} + \frac{Ll^2}{EI}\right) F_x + \left(\frac{3L^2 l}{2EI} + \frac{Ll^2}{2EI}\right) P - \left(\frac{l^2}{2EI} + \frac{Ll}{EI}\right) M \\ D_y = \int_0^L \frac{M_1(x)}{EI} \frac{\partial M_1}{\partial P} dx + \int_0^L \frac{M_2(x)}{EI} \frac{\partial M_2}{\partial P} dx + \int_0^L \frac{M_3(x)}{EI} \frac{\partial M_3}{\partial P} dx \\ \quad = \left(\frac{L^2 l}{2EI} + \frac{3Ll^2}{2EI}\right) F_x + \left(\frac{l}{EA} + \frac{8L^3}{3EI} + \frac{lL^2}{EI}\right) P - \left(\frac{2L^2}{EI} + \frac{Ll}{EI}\right) M \\ 0 = \int_0^L \frac{M_1(x)}{EI} \frac{\partial M_1}{\partial P} dx + \int_0^L \frac{M_2(x)}{EI} \frac{\partial M_2}{\partial P} dx + \int_0^L \frac{M_3(x)}{EI} \frac{\partial M_3}{\partial P} dx \\ \quad = -\left(\frac{l^2}{2EI} + \frac{Ll}{EI}\right) F_x - \left(\frac{2L^3}{EI} + \frac{lL}{EI}\right) P - \left(\frac{2L^2}{EI} + \frac{l}{EI}\right) M \end{cases} \quad (2.2)$$

where  $E$  is the Young's Modulus,  $\alpha$  is the thermal expansion coefficient,  $\Delta T$  is the average temperature change in beams,  $A$  is the cross sectional area of the beam,  $I$  is the beam moment of inertia. Therefore, if let the virtual force  $P$  equal to zero, the displacement and generated force of the ZTA can be calculated.

The deflection  $D$  in the shuttle tip can be written as

$$D = \frac{12\alpha\Delta TL^3}{l^2 + 6L(l + \frac{W^3}{3l})} \quad (2.3)$$

where  $\alpha$  is the thermal expansion coefficient,  $\Delta T$  is the average temperature increase in the beams which is able to be expressed as Equation (2).  $L$ ,  $l$ , and  $W$  are the length of Z-shaped beams, length of the eccentricity, and width of the beams, respectively, as indicated in Figure 2.1. The average temperature ( $\Delta T$ ) is given by

$$\Delta T = \frac{V^2}{12k_p\rho} \quad (2.4)$$

where  $V$  is the applied voltage,  $k_p$  is the thermal conductivity,  $\rho$  is the resistivity of the device. The heat convection and radiation are neglected here for average temperature calculation. And since the underneath of the ZTA is completely etched as a hole (shown in Figure 2.1) due to the SOIMUMPs process [43], the heat conduction to the substrate through the underneath air layer does not occur either.

The stiffness  $k$  of the device can be calculated as

$$k = \frac{2EW^3h(l^3 + 2LW^2 + 6Ll^2)}{(8L^3l^3 + W^2l^4 + 16W^2L^4 + 2W^4Ll + 12L^4l^2 + 6W^2Ll^3)} \quad (2.5)$$

where  $E$  is the Young's Modulus,  $h$  is the thickness of the ZTA.

The output force  $f$  of the ZTA is able to be computed as the product of the deflection and the stiffness based on Hooke's Law, namely

$$f = kD \quad (2.6)$$

Comparing with other thermal actuators frequently used, ZTAs have distinct advantages. The ZTAs share many features in common with the V-shaped ones, such as less space occupied, rectilinear motion generated, etc. They possess a large range of stiffness and output force that is in between those of the comb drives and V-shaped thermal actuators, thus fill the

gap between these two well-established actuators. In particular, they can achieve smaller stiffness without buckling. Note that the stiffness of the ZTA scales approximately with the square of the beam width, while for V-shaped actuator stiffness almost does not change with the width.

## **2.2 SOIMUMPs Process**

The ZTAs were fabricated at MEMSCAP (Durham, NC) using the SOI-MUMPs (Silicon on Insulator – Multi User MEMS Process) [43]. The structure layer is n-type (phosphorus) doped single crystalline silicon (SCS). The SOIMUMPs process is a 4-mask level SOI patterning and etching process. The 4 mask levels are PAD METEL, SOI, TRENCH, and BLANKET METAL, respectively. It has 4 material layers (after etching away the sacrificial layer, i.e. Bottom Oxide) (Figure 2.3 (a)), namely Metal (including Pad Metal with 0.52  $\mu\text{m}$  thickness and Blanket Metal with 0.65  $\mu\text{m}$  thickness), Silicon (10  $\mu\text{m}$  thickness), Oxide (1.0  $\mu\text{m}$  thickness), and Substrate (400  $\mu\text{m}$  thickness).

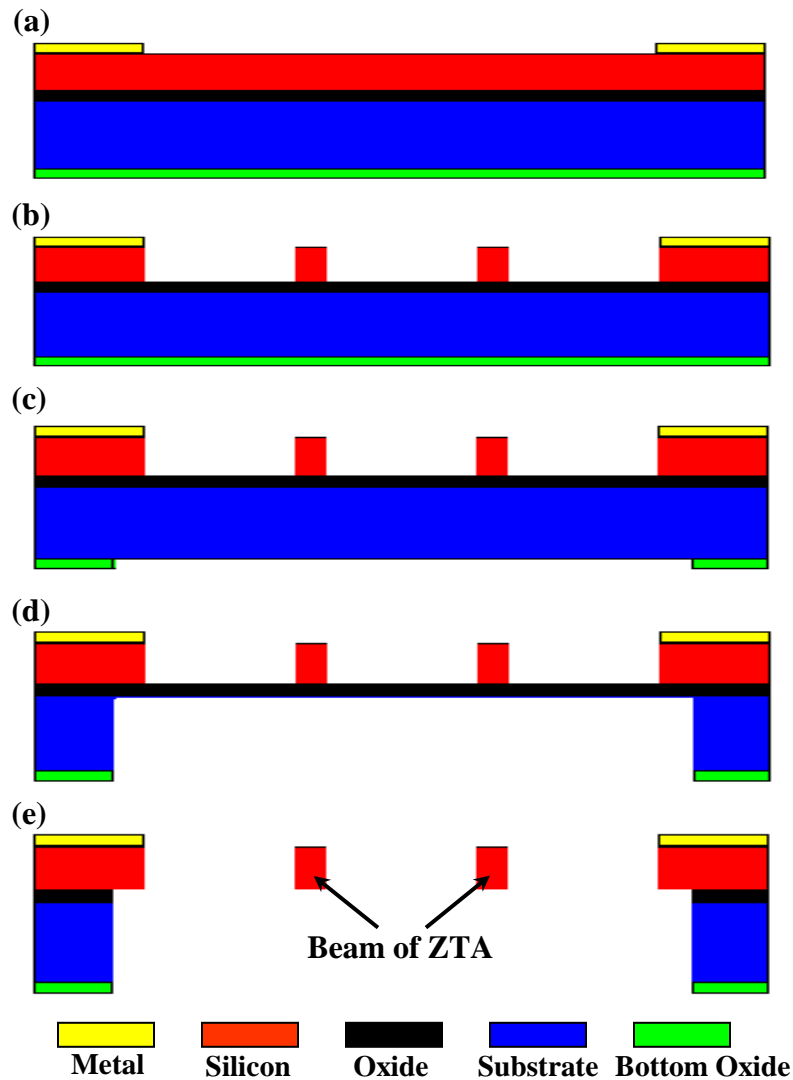


Figure 2.3 SOIMUMPs fabrication highlighted processing features

The SOIMUMPs fabrication flow chart of key steps is shown in the Figure 2.3 (masks are not shown here). In the beginning of the fabrication, the top surface of the Silicon layer is doped by PSG (Phosphosilicate Glass) and then removed by wet comical etching after annealing at 1050°C for one hour in Ar, which is not shown in the Figure 2.3. By liftoff process, the Metal layer (20 nm of chrome and 300 nm of gold) is deposited on the surface over the photoresist pattern that is patterned by exposing the photoresist with light through the first level mask (PAD METAL). The function of this Metal layer is providing electric connection and conduction (Figure 2.3(a)). After that, the photoresist is dissolved. The UV

(ultraviolet) light sensitive photoresist then is lithographically patterned and exposed to UV light through the second level mask (SOI). Therefore, the exposed area of photoresist is removed, and the leaving region is treated as the mask for structure etching. Then, Silicon layer is etched down to the Oxide layer using deep reactive ion etching (DRIE) to obtain the device structure (Figure 2.3(b)) depending upon the mask of leaving photoresist. This mask then is chemically removed after etching. After coating the front side a protection material, the wafers are reversed for developing the backside. The Bottom Oxide layer firstly is patterned with photoresist using the third mask level (TRENCH). Reactive ion etching is then used to move away the exposed Bottom oxide layer (Figure 2.3(c)). Substrate layer is subsequently etched away by DRIE completely stopping by the Oxide layer (Figure 2.3(d)). A wet oxide etching is used to remove Oxide layer (Figure 2.3(e)). After removing the backside photoresist, the wafers are reversed again to make the front side to the top. Remaining bared Oxide layer is then etched from top surface using a vapor HF process after removing the front side protection layer. The device now is free to move without substrate. Finally, the shadow mask is prepared by the METAL mask separately and aligned to the SOI layer. Based on this mask, Blanket Metal layer (with 50 nm Cr+ and 600 nm Ay) is deposited on the top surface of the SOI layer. After evaporation, the shadow mask is removed.

## 2.3 Static Response

### 2.3.1. Multiphysics Simulation

The nonlinear multiphysics simulation is performed to analyze the static response of the ZTA in vacuum condition using ANSYS 11.0. This coupled-field analysis includes electrical, thermal and mechanical fields. And the simulation is to mimic the static response of the device under condition of vacuum and room temperature.

The dimensions of the ZTA (the same as those in experiments) and the temperature dependant material parameters used in the simulations are listed in the Tables 2.1 and 2.2, respectively. The element type for the multiphysics simulation used in ANSYS is *Solid 226* that is a 3-D element type for thermal-electro-structural analysis.

Table 2.1 Dimensions of the Z-shaped thermal actuator used in simulations.

Dimension	Symbol	Value	Unit
Beam length	$L$	88	$\mu\text{m}$
Beam width	$W$	4	$\mu\text{m}$
Thickness	$h$	10	$\mu\text{m}$
Eccentricity	$l$	20	$\mu\text{m}$
Shuttle length	$L_S$	92	$\mu\text{m}$
Shuttle width	$W_S$	60	$\mu\text{m}$

Table 2.2 Material parameters used in simulations.

Parameter	Symbol	Value	Unit
Young's modulus	$E$	160	GPa
Poisson's ratio	$\nu$	0.28	-
Thermal conductivity (constant)	$K$	146	W/(mK)
Thermal conductivity (temperature dependant)	$K(T)$	$210658 \times T^{-1.2747}$	W/(mK)
Thermal expansion coefficient (constant)	$\alpha$	$2.5 \times 10^{-6}$	$\text{K}^{-1}$
Thermal expansion coefficient (temperature dependant)	$\alpha(T)$	$-4 \times 10^{-12} T^2 + 8 \times 10^{-9} T + 4 \times 10^{-7}$	$\text{K}^{-1}$
Resistivity (constant)	$\rho$	$5.1 \times 10^{-5}$	$\Omega\text{m}$
Resistivity (temperature dependant)	$\rho(T)$	$5.1 \times 10^{-5} [1 + 3 \times 10^{-3} (T - 273)]$	$\Omega\text{m}$
Piezoresistance coefficients	$\pi_{11}$	$-15 \times 10^{-11}$	$\text{Pa}^{-1}$
	$\pi_{12}$	$7.5 \times 10^{-11}$	$\text{Pa}^{-1}$
	$\pi_{44}$	$-12 \times 10^{-11}$	$\text{Pa}^{-1}$

For the boundary conditions of the simulation, since both ends of the beams are fixed to the anchors to limit the motions and rotations,  $U_x = U_y = U_z = R_x = R_y = R_z = 0$ . Furthermore, the thermal boundary conditions are zero temperature change at the anchors. The input of the simulation was applied current across the beam ranging from 0 to 9.5 mA. Because, in real experiment, if the applied current is too high (e.g. over 10 mA), the recrystallization [44] would happen and so that damage the device. Thus we kept the applied currents less than 10 mA in all our simulations and experiments. The outputs included ZTA voltage (to calculate resistance), temperature and displacement distributions.

Figure 2.3(a), 2.3(b) and 2.3(c) are showing the displacement, temperature and voltage distribution of the ZTA at the applied current of 8.5 mA, respectively. The highest temperature occurs on the center shuttle part since the shuttle is the farthest from the anchors. And the shuttle attains the highest displacement since the symmetric structure of the device and thermal expansion effect.

The simulation results for the center shuttle deflection, temperature change and the voltage distribution along the device versus applied current are shown in Figure 2.4(a), (b) and (c). The simulation results will be validated by experiments. However, since the temperature distribution measurement is difficult to operate in vacuum. Therefore, the temperature simulation results would compare with the experimental results under air condition.

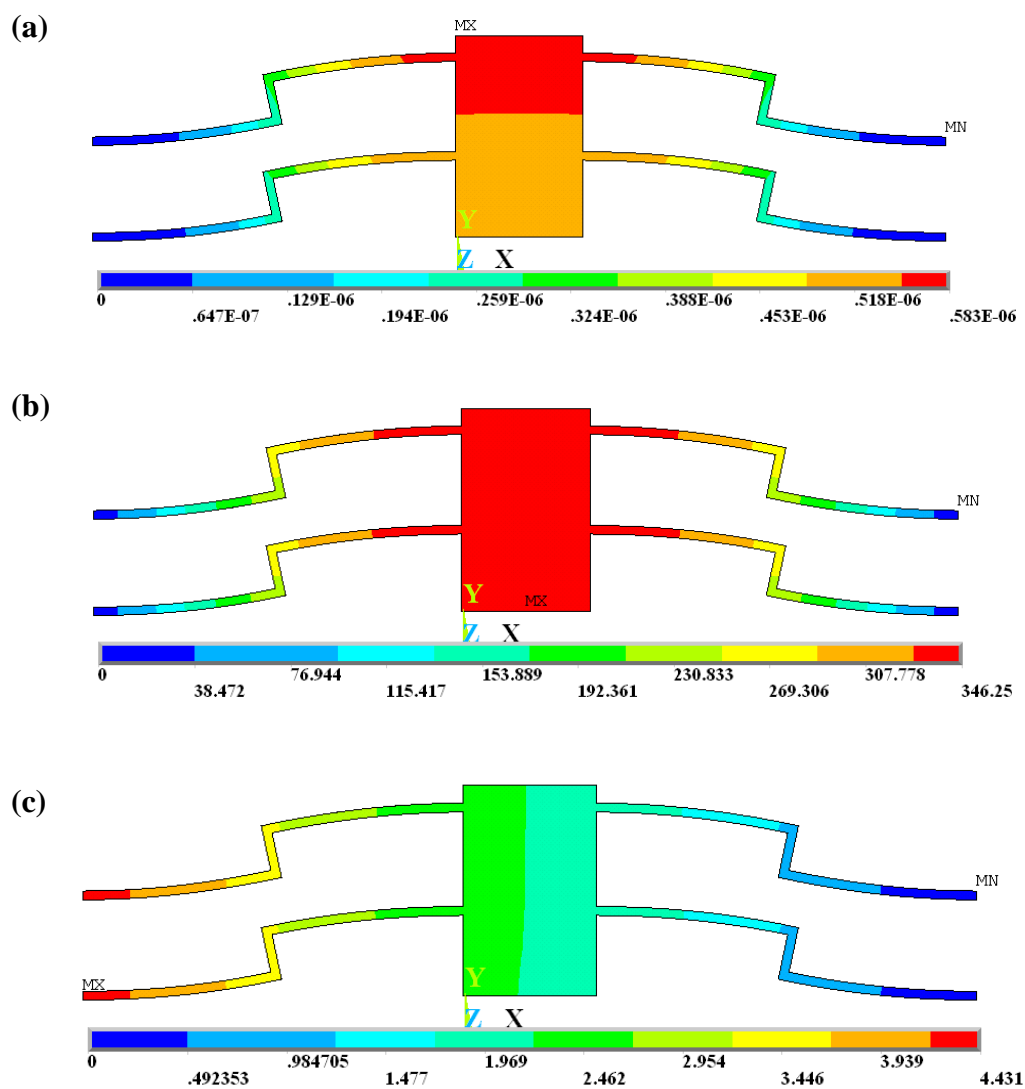
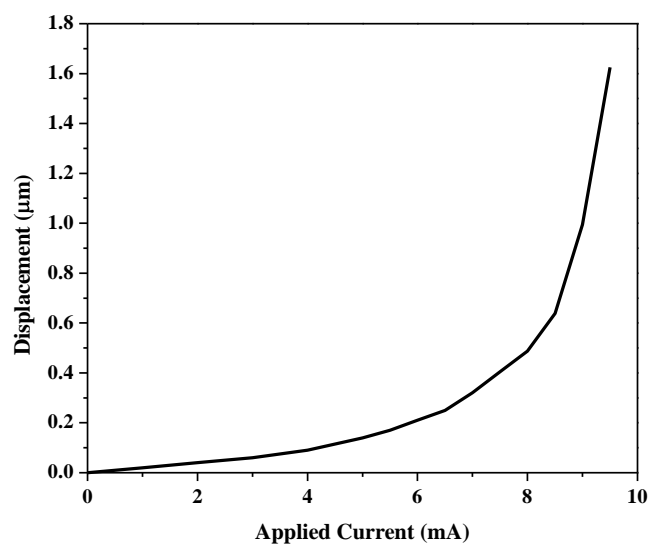
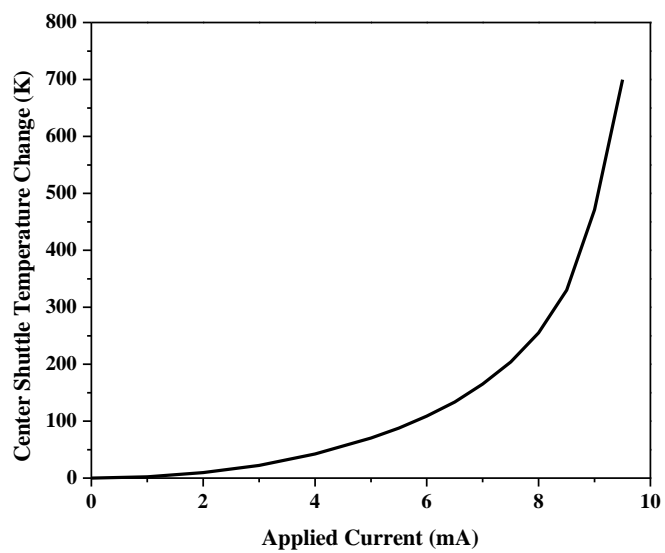
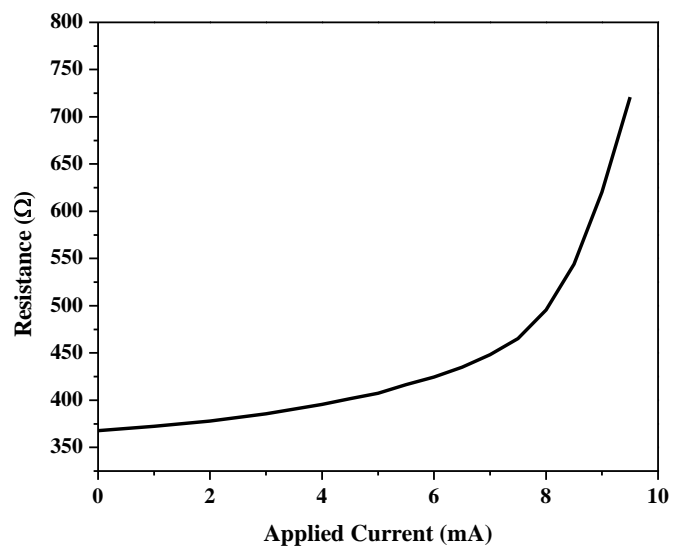


Figure 2.4 Simulation results at 8.5 mA. (a) The displacement distribution of ZTA at the 8.5 mA current level. The unit is in micro-meter. (b) The temperature distribution of ZTA at the 8.5 mA current level. The unit is in Kelvin. (c) The voltage distribution of ZTA at the 8.5 mA current level. The unit is in Volt.

Figure 2.5 The multiphysics simulation results. (a) The displacement simulation results. (b) The shuttle temperature simulation results. (c) The resistance (converted by output voltage results) simulation results.

**(a)****(b)**

(c)



### 2.3.2. Experimental Results

The static response of the ZTA with the dimensions shown in Table 2.1 was tested in vacuum environment and room temperature condition to validate the simulation results. And the tests were carried out inside an SEM (JEOL6400F). The deflections of ZTA were measured from the SEM images with a resolution of 4.6 nm.

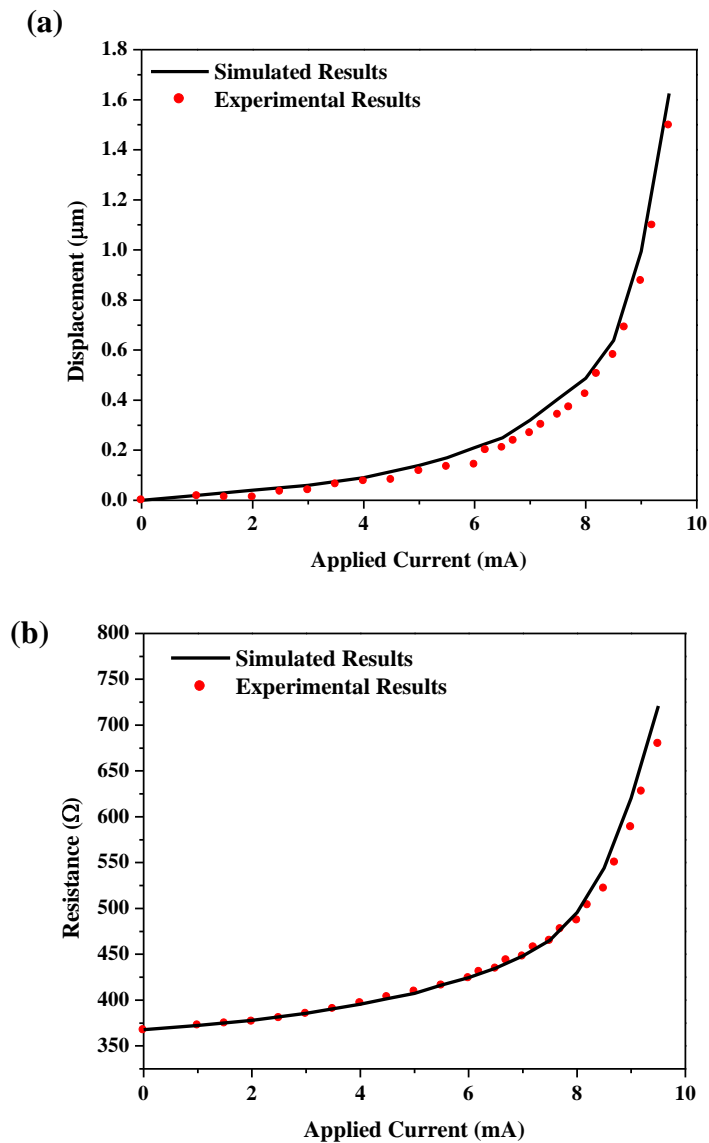


Figure 2.6 The experimentally static response of the ZTA comparing with simulated results (a) Displacement as functions of applied current. (b) Resistance as functions of applied current.

The deflection of the shuttle was measured with the actuation current from 0 to 9.5 mA. The experimental results are shown in Figure 2.6 comparing with the simulated results. Figure 2.6(a) shows that at low applied current (0 to 6 mA), the ZTA's displacement would not change much with the current rise. And the relation is approximately linear. However, the ZTA can achieve relatively large deflection when applied current is higher 6 mA. This large deflection of the center shuttle is because the geometry of the ZTA amplifies the relatively small thermal expansion in beams. We also tested the V-I relationship of the device and converted it to resistance based on Ohm's Law. And the resistance versus applied current is shown in Figure 2.6(b). The initial resistance without apply any external power is 367.3  $\Omega$ . From Figure 2.6(b), it indicates that the resistance has the same change trend as the displacement. Initially, the resistance increases only 10  $\Omega$  when current increased 6 mA. However, when current was over 6 mA, the resistance changes dramatically. This is because the resistivity of the single crystalline silicon is changing with the temperature.

## 2.4 Dynamic Response

In a thermal actuator, there are three modes of temperature transfer, conduction, convection and radiation. However, the static response results are showing, in our experiment, the temperature increase, at most, to 1000 K (room temperature considered). Therefore, the heat dissipation through radiation to the ambient is negligible. The chip we were using was SOI, therefore, no substrate underneath. The heat loss through the surface area to the substrate is also neglected. A simple model for heat transfer was used to evaluate the temperature of the thermal actuator as Figure 2.7 shown. Because the thermal actuator is long enough comparing with its thickness and width, the one dimensional analysis of the heat flow was performed. If we just consider the center part of the plate with the length  $dx$  shown in Figure 2.7, three factors will affect the temperature of this part, namely the temperature transferred from the previous part, the temperature transferred to the next part, and the generation heat of itself. Therefore, the temperature on this part can be expressed as

$$\tau_s \frac{\partial T}{\partial t} = k_p A \frac{\partial T}{\partial x} \Big|_x - k_p A \frac{\partial T}{\partial x} \Big|_{x+\Delta x} + J^2 \rho A dx \quad (2.7)$$

where  $\tau_s$  is the time required for temperature reaching the stable status.  $\frac{\partial T}{\partial t}$  is the temperature change rate,  $k_p$  is the thermal conductivity,  $A$  is the cross-sectional area,  $J$  is the current density,  $\rho$  is the resistivity.

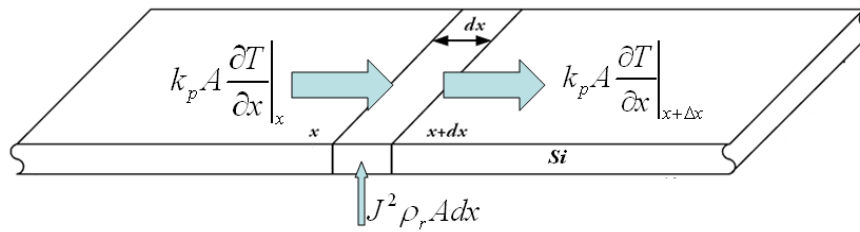


Figure 2.8 Cross section of the actuator for thermal analysis.

According to [45], the temperature change is equal to

$$\frac{dT}{dt} = \frac{k_p}{C \rho_s} \frac{d^2 T}{dx^2} + \frac{V^2 / R}{C \rho_s A L} \quad (2.8)$$

where  $C$  and  $\rho_s$  are the specific heat and the density of single crystalline silicon, respectively.  $R$  is the resistance of the structure we are analyzing,  $L$  is the length of the analyzed part. Therefore,  $\tau_s$  can be calculated as 65  $\mu s$ . Consequently, time constant is

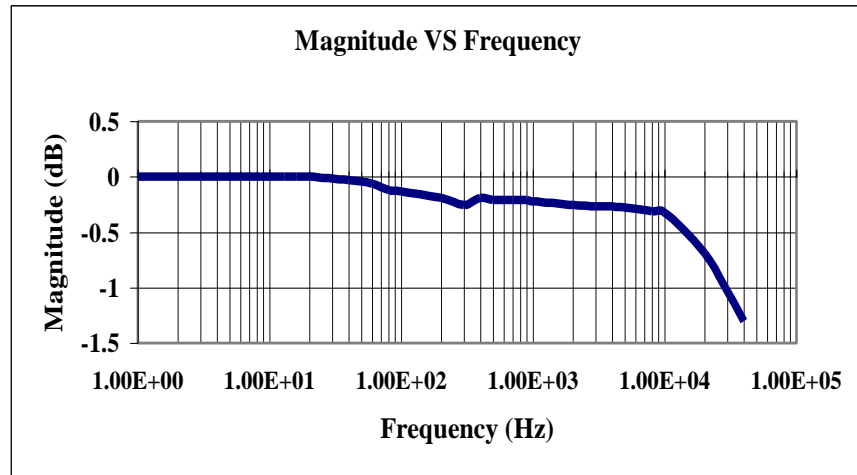
$$\tau_{TC} = 65 \mu s \times 63.3\% = 41.145 \mu s \quad (2.9)$$

The resistance dynamic response of the ZTA was tested. The dynamic response testing was performed experimentally in the same environmental condition as static response testing. The input was applied from function generator (Agilent, 33250A). The function generator can only generate voltage signal, therefore, the digit multimeter was used to obtain the effective output current (i.e. Root Mean Square value). The ZTA was driven by the signal with the magnitude of 4 V and the frequency ranging from 5 to 40k Hz. The phase transfer of the ZTA was detected by Lock-in Amplifier (SR 830). The reference signal was sent out directly from Sync port of function generator so that the frequency would be equal to the

actuation frequency of ZTA. Figure 2.7 shows the bode plot of the frequency response of the ZTA.

The steep magnitude drops-off at about 50 Hz firstly. This change is in the same frequency range reported in [2] for displacement dynamic measurement. Because the displacement is due to the thermal expansion and the temperature change is because of the resistivity change. Therefore, if the resistance changes, the displacement should also follows. Then the resistance is tending to be stable. However, when the frequency increases higher than 10 kHz, the resistance decreases dramatically results from the heat transfer dynamics of the ZTA. The ZTA is a temperature dependent device. After the voltage applied to the device, the ZTA needs time to be heated up and cooled down for moving forward and back. In addition, the resistivity of the SCS is also temperature dependent. It would accordingly change with the temperature. However, the temperature change of the ZTA cannot response as fast as the voltage change when the frequency frequency of the applied voltage increases gradually and rises over a critical value. The resistivity, thereby, will gradually decrease.

(a)



(b)

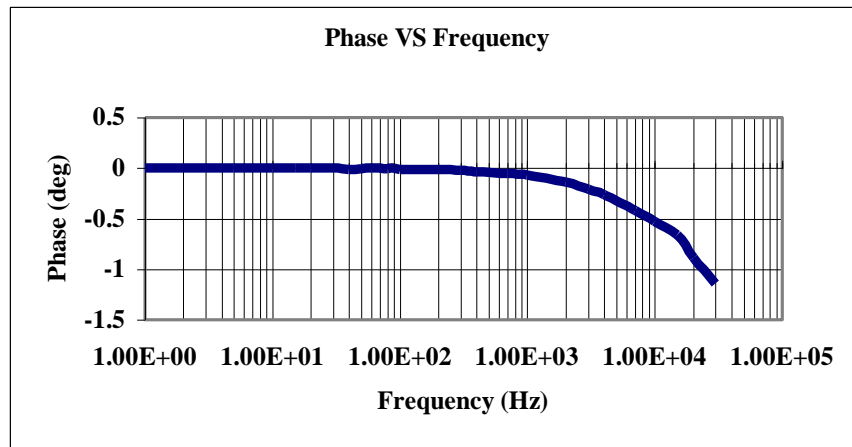


Figure 2.9 Dynamic response of the ZTA. (a) Magnitude versus frequency. (b) Phase versus frequency.

## Chapter 3 Piezoresistive Effect Experiment

Two effects can result in resistance change in a ZTA, namely, temperature change and piezoresistivity [46]. The temperature change is mainly due to the input actuation change. The resistance rises as its applied current increases has shown in Figure 2.6. With an external force, the resistance at the given current further changes due to the piezoresistive effect.

### 3.1 Piezoresistive self-sensing of the ZTA

#### 3.1.1 Experimental Measurement of Piezoresistivity

To test the resistance change due to the piezoresistive effect only, a given current of the ZTA was maintained constant while an external force was exerted to the ZTA. A tungsten probe (Model 7B-2, Micromanipulator) attached to a nanomanipulator (Klocke Nanotechnik, Aachen, Germany) inside SEM was used to push the ZTA in the opposite direction of its movement. The probe was positioned in the middle of the shuttle (guided by SEM imaging) to prevent in-plane rotation of the ZTA. For each given current and external force, the voltage (thus resistance) and displacement of the ZTA were recorded in the following procedure. Then different values of current and external force were repeated.

1) The initial position  $P_0$  (i.e., the distance between the shuttle of the ZTA and the tungsten probe, where the tungsten probe served as a reference point) was recorded. The displacement of the ZTA was set as zero. The initial resistance of the ZTA was recorded as  $R_0$ .

2) A current ( $I_1$ ) was applied across the ZTA. The actuated position ( $P_1$ ) and the output voltage ( $V_1$ ) were recorded.  $D_1 = P_0 - P_1$  is the displacement of the ZTA at current  $I_1$ . The resistance ( $R_1$ ) was calculated by the Ohm's Law. The resistance change  $R_1 - R_0$  is due to the temperature effect.

3) The current was turned off, and the tungsten probe was moved towards the ZTA with a gap  $G_1$  between them (smaller than  $D_1$ ) (Figure 3.1(a)).

4) The same current  $I_1$  was turned on again. The ZTA moved  $G_1$  due to the blocking of the tungsten probe (Figure 3.1(b)). The output voltage ( $V_2$ ) was recorded to compute the resistance  $R_2$ . The resistance change  $R_2 - R_1$  is due to the external force exerted by the tungsten probe. Note here the ZTA displacement was  $G_1$  and the external force was  $F = (D_1 - G_1) \times k$ , where  $k$  is the stiffness of the ZTA. Therefore, the resistance value under a given current and a given external force was obtained.

5) Steps 3) and 4) were repeated with different gaps between the tungsten probe and the ZTA ( $G_2, G_3, G_4$  and etc.) at the same current ( $I_1$ ) to obtain more external forces (and ZTA displacements) for this given current.

6) Steps 2) to 5) were repeated with different current levels ( $I_2, I_3, I_4$  and etc.) until sufficient data points were acquired.

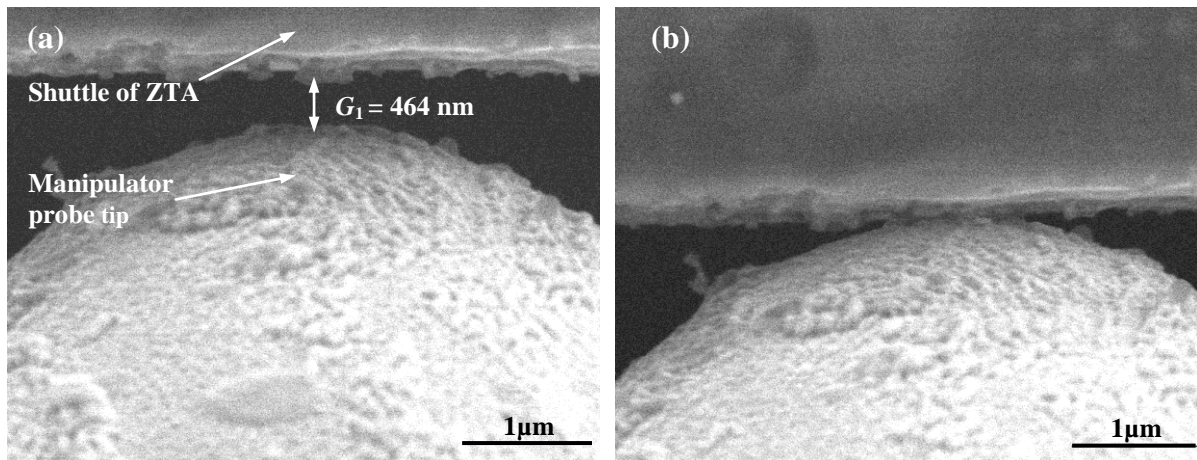


Figure 3.1 The experimental process for the piezoresistivity measurement. (a) The gap between the ZTA and the manipulator probe tip is less than  $D_1$  (581 nm at  $I_1 = 8.6$  mA) to block the ZTA movement. (b) The probe pushes the ZTA back by 117 nm after  $I_1$  is applied again to the ZTA.

Two assumptions are made in the above experiments and data analysis. First, the tungsten probe does not affect the temperature profile of the ZTA at a given current when they are in contact. A ceramic thermal insulator layer is placed between the tungsten probe

and the nanomanipulator base. Second, the tungsten probe is treated as a rigid body in view that its stiffness is much larger than that of the ZTA. These assumptions will be checked with finite element analysis (FEA) (to be described).

### 3.1.2 Experimental Results of Piezoresistivity

All experiments were carried out inside a SEM (JEOL 6400F) under vacuum and room temperature. The displacements and gaps were measured from the SEM images with a resolution of 4.6 nm. The initial resistance (under room temperature) and the stiffness of the ZTA were 367.3  $\Omega$  and 274.3 N/m, respectively.

In our experiments, the data were collected for the applied current ranging from 6.0 to 9.5 mA. When the current is smaller than 6.0 mA, the displacement of the ZTA is very small ( $< 200$  nm), which presents a challenge to precisely control the gap between the ZTA and the tungsten probe. On the other hand, if the applied current is very high (e.g.,  $>10$  mA), recrystallization of SCS could occur [46] as discussed in Chapter 2.

The experimental results are shown from Figure 3.2 to 3.4. Under different current levels, the output voltage ( $V_2$ ) is plotted as a function of the external force in Figure 3.2(a). In the experiments, the direction of the external force was opposite to the moving direction of the ZTA, which is set as positive. Note that at the same current level, the resistance ( $R_2$ ) (obtained from voltage shown in Figure 3.2(a)) decreased with the increase of the external force, due to the piezoresistive effect. As shown in Figure 3.2(a), at 8.6 mA current level, for instance, the output voltage linearly decreased from 4.114 to 4.086 V (i.e., the resistance decreased from 478.4 to 475.1  $\Omega$ ) when the external force increased from 0 to 128.65  $\mu\text{N}$ . For a given current level, an unloaded ZTA reached its maximum displacement. Applying an external force while maintaining the same current, therefore, increases the compressive stresses in the beams, which in turn induces the decrease in voltage due to the piezoresistive effect. Figure 3.2(b) plots the relationship between the measured displacement of the ZTA and the output voltage. Figures 3.2(a) and (b) show that the ZTA can be used to sense both external force and displacement by measuring the output voltage.

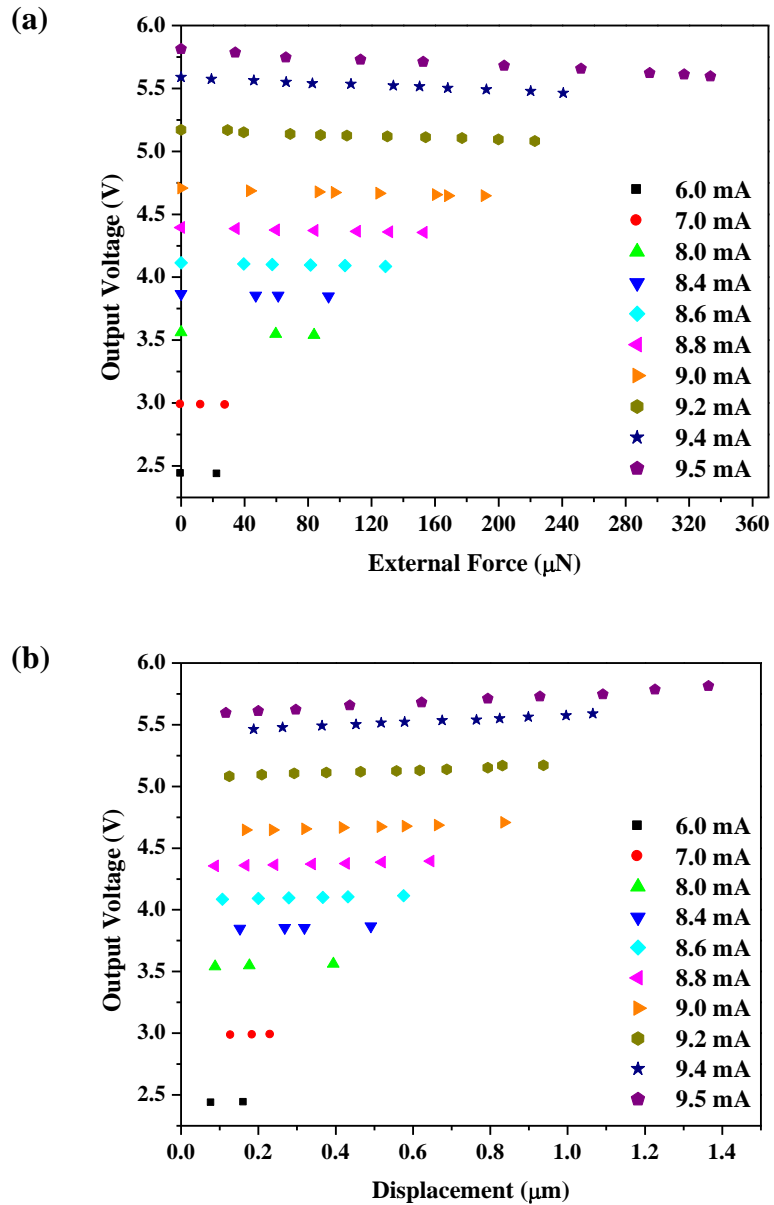


Figure 3.2 (a) Voltage versus external force for all current levels. For each current, the external force starts as zero (no applied force) and increases. (b) Voltage versus displacement for all current levels.

The sensitivity  $\alpha$ , defined as the slope of the linear fitting under each applied current level in Figure 3.2(a), varies with the applied current, as shown in Figure 3.3. The negative value of the sensitivity means that when the external force increases, the output voltage decreases. The sensitivity levels off initially and increases sharply when the current is over

8.6 mA. For example, at the current level of 8.6 mA, when the ZTA is pushed back by an external force of 1  $\mu\text{N}$ , the output voltage and resistance decreases by 0.22 mV and 25.4  $\text{m}\Omega$ , respectively. The resolution of the force sensor is ultimately determined by the noise level.

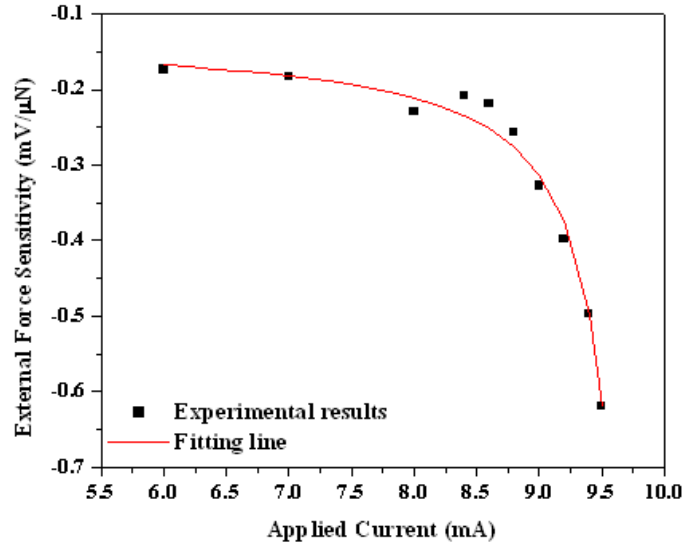


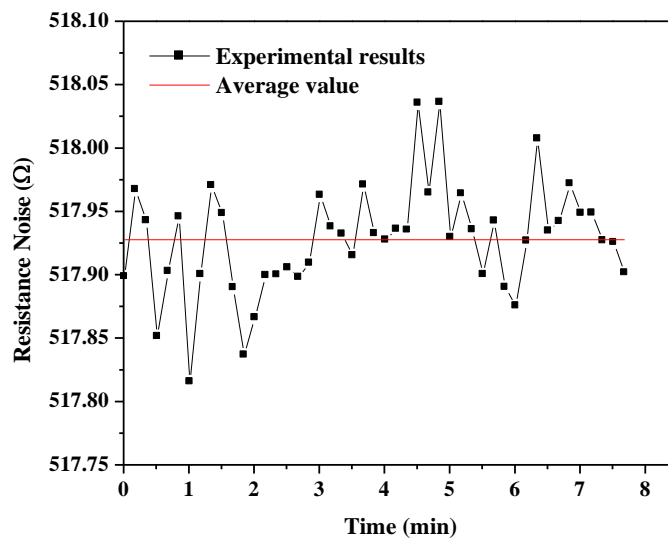
Figure 3.3 The external force sensitivity at different current levels.

Figure 3.4 shows the resistance fluctuation at 8.6 mA current in 8 minutes. The noise can be quantified by the root mean square deviation (RMSD) of the experimental data, viz.,

$$R_n = \sqrt{\frac{\sum_{i=1}^N (R_i - \bar{R})^2}{N}} \quad (3.1)$$

where the  $R_n$  is the resistance noise,  $R_i$  is the data point,  $\bar{R}$  is the average value,  $N$  is the number of the data. The resistance noise was 0.043  $\Omega$  at 8.6 mA according to Equation 3.1. The noise is possibly due to stray electromagnetic fields present inside the chamber, stage vibration or exposure to the electron beam. Based upon the measured sensitivity and noise, the resolution of the force sensor is given by  $\frac{R_n I}{|\alpha|}$ , where  $I$  is the applied current. The load

resolution of  $1.68 \mu\text{N}$  at  $8.6 \text{ mA}$  current was obtained. Note that the load resolution can be substantially improved by reducing the stiffness of the ZTA.



**Figure 3.4** Noise of the resistance at the applied current of  $8.6 \text{ mA}$ . The red line is the average value of all the data points.

### 3.2 Multiphysics FEA

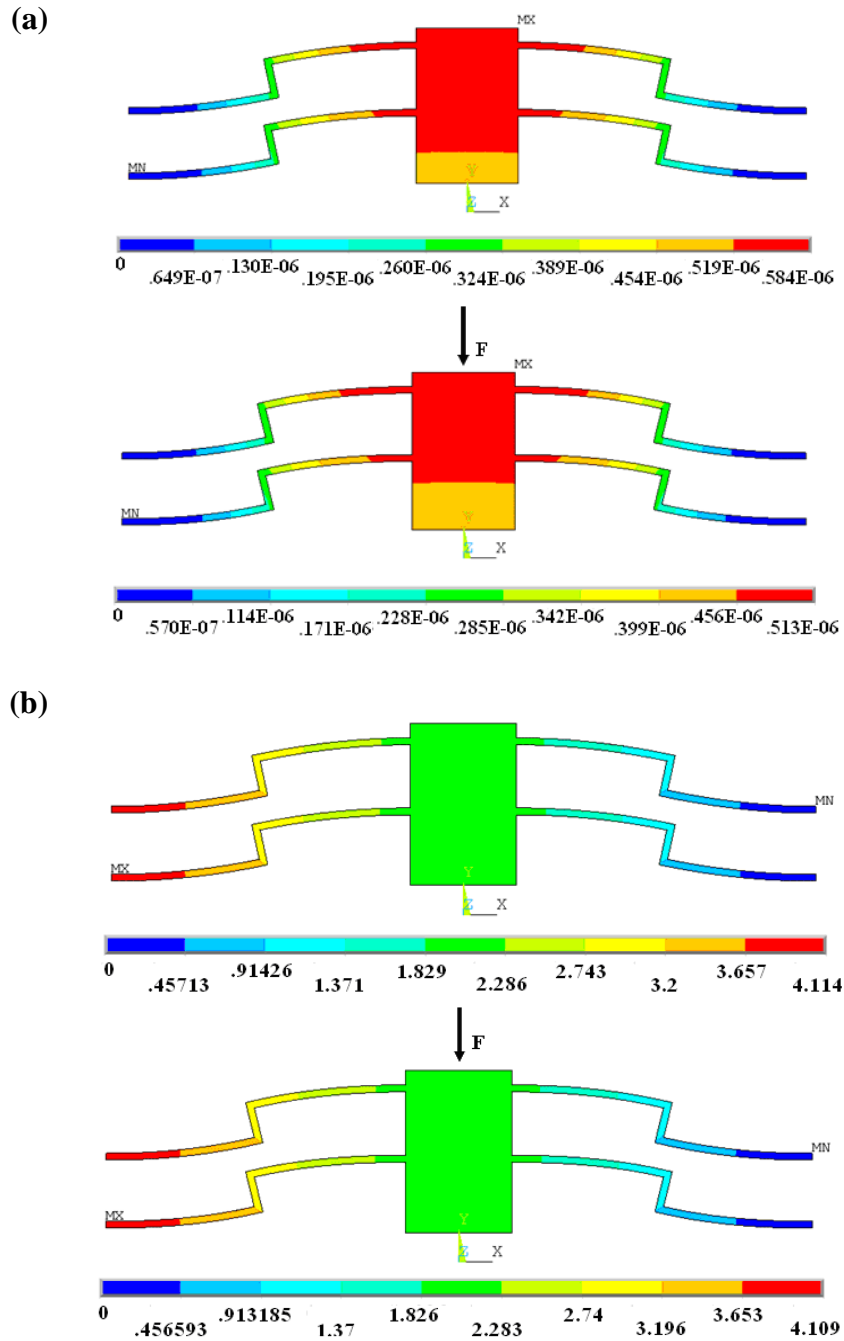


Figure 3.5 The simulation results at the 8.6 mA current level with the external force of 20  $\mu\text{N}$ . (a) Displacement of the shuttle changes from 0.584  $\mu\text{m}$  to 0.513  $\mu\text{m}$ . (b) Output voltage changes from 4.114 V to 4.109 V.

To validate the assumptions in the experiments, nonlinear multiphysics simulations using ANSYS 11.0 were performed. The dimensions of the ZTA (the same as those in experiments) and the material parameters used in the simulations are as the same as listed in the Table 2.1 and Table 2.2, respectively. The three piezoresistance coefficients ( $\pi_{11}$ ,  $\pi_{12}$ , and  $\pi_{44}$ ) are dependent on several factors including temperature, doping concentration, original bulk resistivity, crystalline structure, and surface concentration of the diffused layer [15;47]. Some of these factors are difficult to measure or quantify. In our work, these coefficients are approximated from [48] and [39] (see Table 2.2). The element type for the multiphysics simulation in ANSYS 11.0 is *Solid 226* that is a 3-D element type for both thermal-electro-structural analysis and piezoresistive analysis. A series of simulations were performed at different currents and external forces. Figure 3.5 (a) and (b) show the simulated displacement and output voltage of the ZTA before and after subjected to an external force of 20  $\mu\text{N}$ , respectively, while the current is maintained at 8.6 mA. When the ZTA is pushed back by 0.071  $\mu\text{m}$  under the 8.6 mA current, the output voltage decreases by 0.005 V.

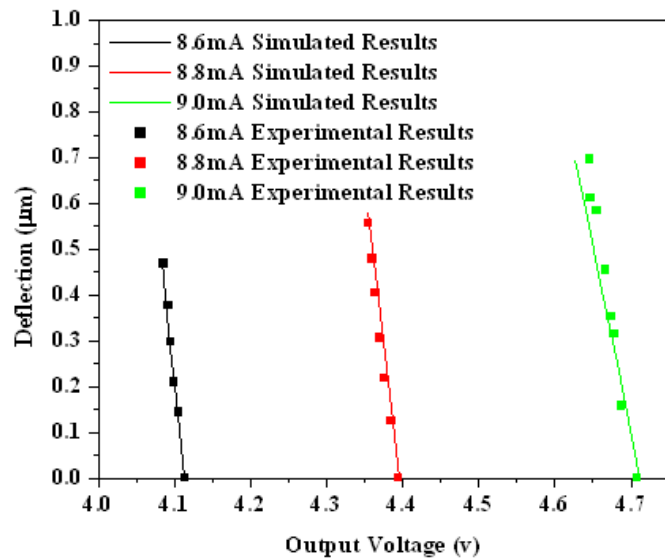


Figure 3.6 The comparison between the simulated and experimental results at 8.6, 8.8 and 9.0 mA current levels. In the multiphysics simulations, temperature-dependent resistivity and thermal expansion coefficient were used (see table 2).

The simulation results agreed very well with the experiments, as shown in Figure 3.6.

## Chapter 4 Feedback Control of the ZTA

A feedback control system based on the piezoresistive sensing characteristics of the ZTA is demonstrated. The function of this feedback control system is that, when the ZTA is pushed by an external force, the feedback system actively updates the current input to compensate the ZTA displacement to the value without the external force (i.e., bring the ZTA to its initial position), while measuring the external force simultaneously.

### 4.1 Data Fitting of the Piezoresistivity Measurements

The ZTA response can be viewed to have two inputs and two outputs; the two inputs are electric current ( $I$ ) and external force ( $F$ ), and the two outputs are displacement ( $D$ ) and electric resistance ( $R$ ) (or voltage,  $V$ ). The relationships between inputs and outputs are plotted in Figure 4.1(a) and (b). A key step is to identify two fitting functions. First of all, the displacement and resistance (when external force is zero) are fitted as functions of the current alone. The best functions we identified are given by

$$D|_{F=0} = \frac{0.14I}{-1.22I + 12.55} \quad (4.1a)$$

$$R|_{F=0} = \frac{-32.77I + 367.26}{-0.096I + 1} \quad (4.1b)$$

Figure 4.2 shows the fittings for both outputs (displacement and resistance). Several material properties, such as thermal conductivity, thermal expansion coefficient and resistivity, are typically temperature dependant (see Table 2.2). This fact determines the types of fit (rational), numerator (linear polynomial) and denominator (linear polynomial).

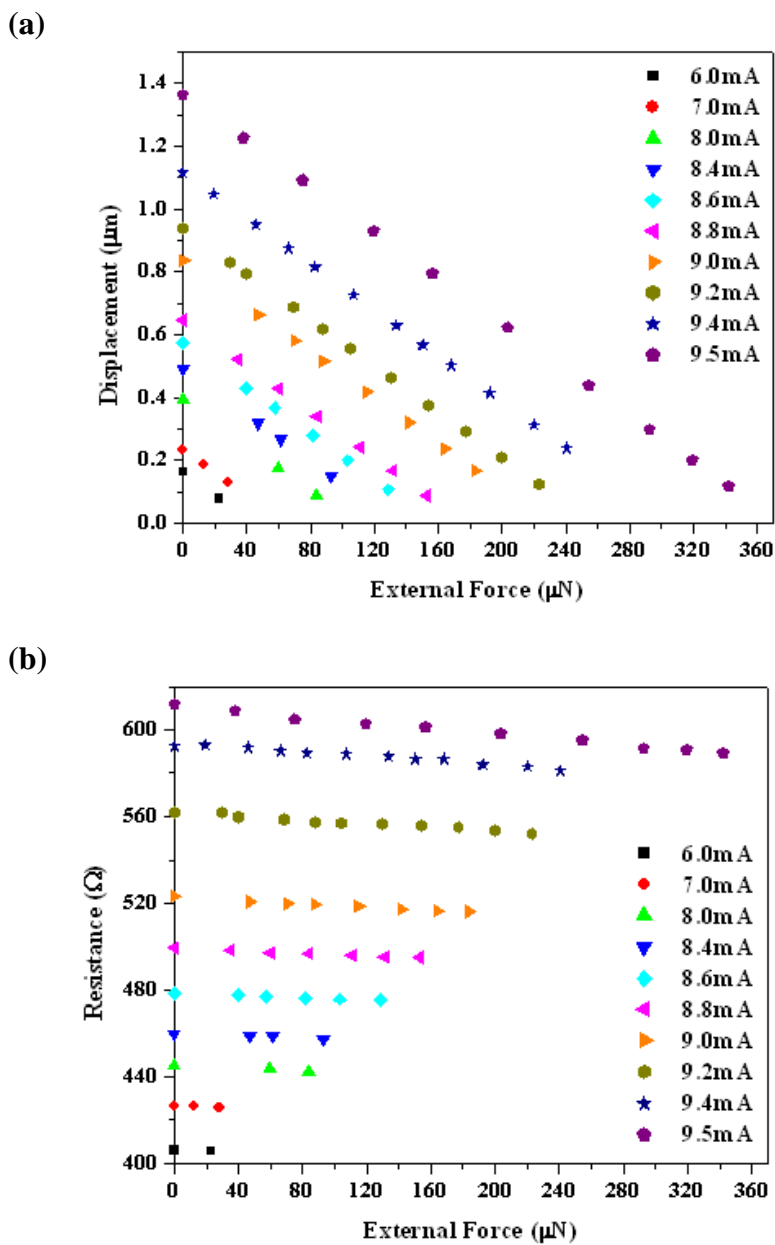


Figure 4.1 (a) The displacement and (b) the resistance change with the external force increasing at different current levels.

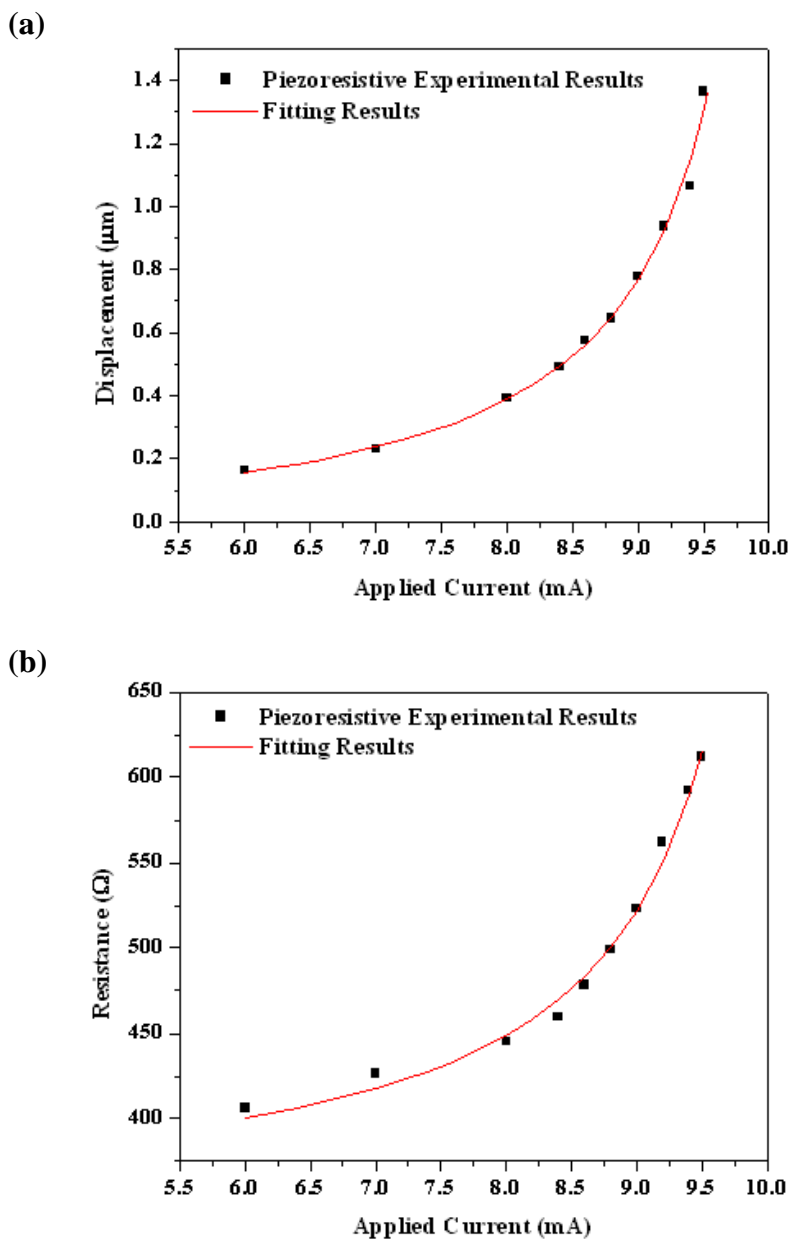


Figure 4.2 Data fitting for (a) displacement and (b) resistance using the piezoresistive experimental results.

Note that the contribution of the current to both the displacement and resistance is independent of the external force. When considering the contribution of the external force, the displacement and resistance are best fitted by

$$D(I, F) = \frac{0.14I}{-1.22I + 12.55} - \frac{F}{274.3} \quad (4.2a)$$

$$R(I, F) = \frac{-32.77I + 367.26}{-0.096I + 1} - \frac{-0.21I + 2.37}{-1.86I + 18.29} \frac{F}{I} \quad (4.2b)$$

The displacement depends on the external force simply following the Hooke's law with the stiffness of the ZTA equal to 274.3 N/m. Such dependence does not change with the current. The resistance also depends on the external force due to the piezoresistive effect. The piezoresistive effect is dependent on the current. As shown in the Figure 3.3, the sensitivity (i.e. the slope of the data points at each current level in Figure 3.2(a)) changes with the current. This is why the second term in Equation 4.2b involves the current. Figure 4.3 shows the fittings for both outputs (displacement and resistance) as functions of the inputs (current and external force).

The accuracy of the above fitting functions was evaluated by the coefficient of determination, which is defined as

$$R^2 = 1 - \frac{SS_{err}}{SS_{tot}}, \quad R^2 \in [0, 1] \quad (4.3)$$

where  $SS_{err} = \sum_{i=1}^n (z_i - \hat{z}_i)^2$  and  $SS_{tot} = \sum_{i=1}^n (z_i - \bar{z}_i)^2$  ( $n$  represents the number of data points,  $z_i$  the measured data,  $\hat{z}_i$  the fitted data, and  $\bar{z}_i$  the mean of the measured data). The coefficients of determination for Equations 4.1a, 4.1b, 4.2a and 4.2b were 0.993, 0.994, 0.991 and 0.991, respectively, which indicated that excellent fittings were indeed obtained.

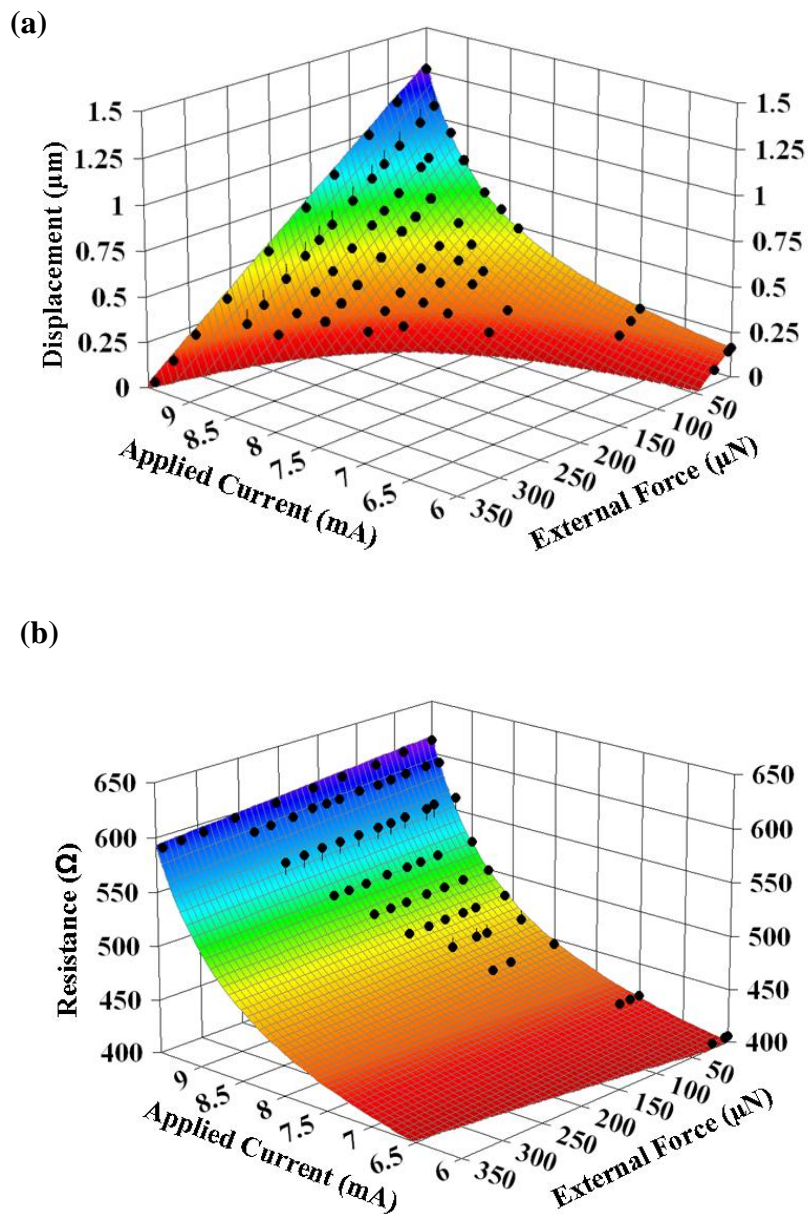


Figure 4.3 (a) Displacement as a function of the applied current and external force. (b) Resistance as a function of the applied current and external force.

## 4.2 Design of Feedback Control System

A feedback control system was built based on the calibrated relationships as shown in Eq. 3. The objective of the feedback system was to, for a given current, maintain the constant displacement under various external forces under quasistatic loading. Here the desired displacement is the set point (for simplicity, when the external force is zero), the sensed resistance is the process variable, the current is the manipulated variable and the external force is the disturbance. The block diagram of the feedback system is shown in Figure 4.4.

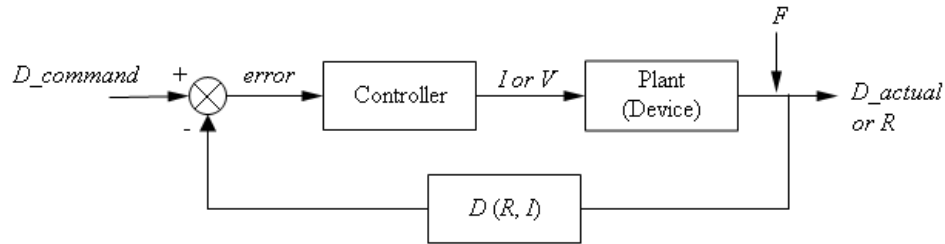


Figure 4.3 Feedback control system with compensator block diagram.

The controller was built in LabVIEW (version 8.5, National Instruments) with a nonlinear algorithm given as

$$\frac{0.14I}{-1.22I + 12.55} + e = \frac{0.14I_0}{-1.22I_0 + 12.55} \quad (4.4)$$

where  $I$  is the updated current,  $I_0$  is the initial current and  $e (= -\frac{F}{274.3})$  is the error between the initial displacement and sensed displacement. The signals of output voltage and updated current were read and written by the computer through a multifunction data acquisition module (DAQ NI USB-6211, National Instruments). The LabVIEW controller works as follows: when an output voltage is read in from the ZTA, the controller converts it to a resistance value based on the given current, and then computes the external force and the sensed displacement according to Equation 4.2b and 4.2a, respectively. The updated current to maintain the displacement is computed by Equation 4.4. The data acquisition module can only read/write voltage signal, hence a simple circuit was built to convert voltage signal to

current signal and vice versa. Figure 4.5 shows the circuit where a dummy resistor ( $1\text{ k}\Omega$ ) is in series with the ZTA.  $V_R$  is the voltage on the dummy resistor. With the measured current ( $=V_R / 1\text{ k}\Omega$ ), the resistance of the ZTA is known by measuring  $V_Z$ .  $V_{out}$  was the voltage output from the data acquisition module (and the LabVIEW program), which was equal to the updated current times the resistance sum of the dummy resistor and the ZTA.

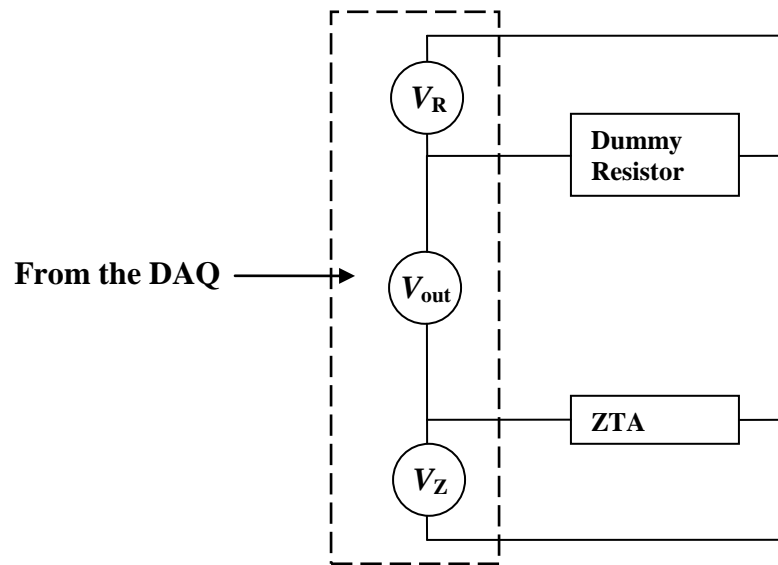


Figure 4.5 Circuit diagram for converting the voltage signal to current signal.  $V_R$  is the voltage on the dummy resistor ( $1\text{ k}\Omega$ ), which is in series with the ZTA. With the measured current ( $=V_R / 1\text{ k}\Omega$ ), the resistance of the ZTA is known by measuring  $V_Z$ .  $V_{out}$  was the voltage output from the data acquisition module (and the LabVIEW program).

### 4.3 Experimental Results of Feedback Control

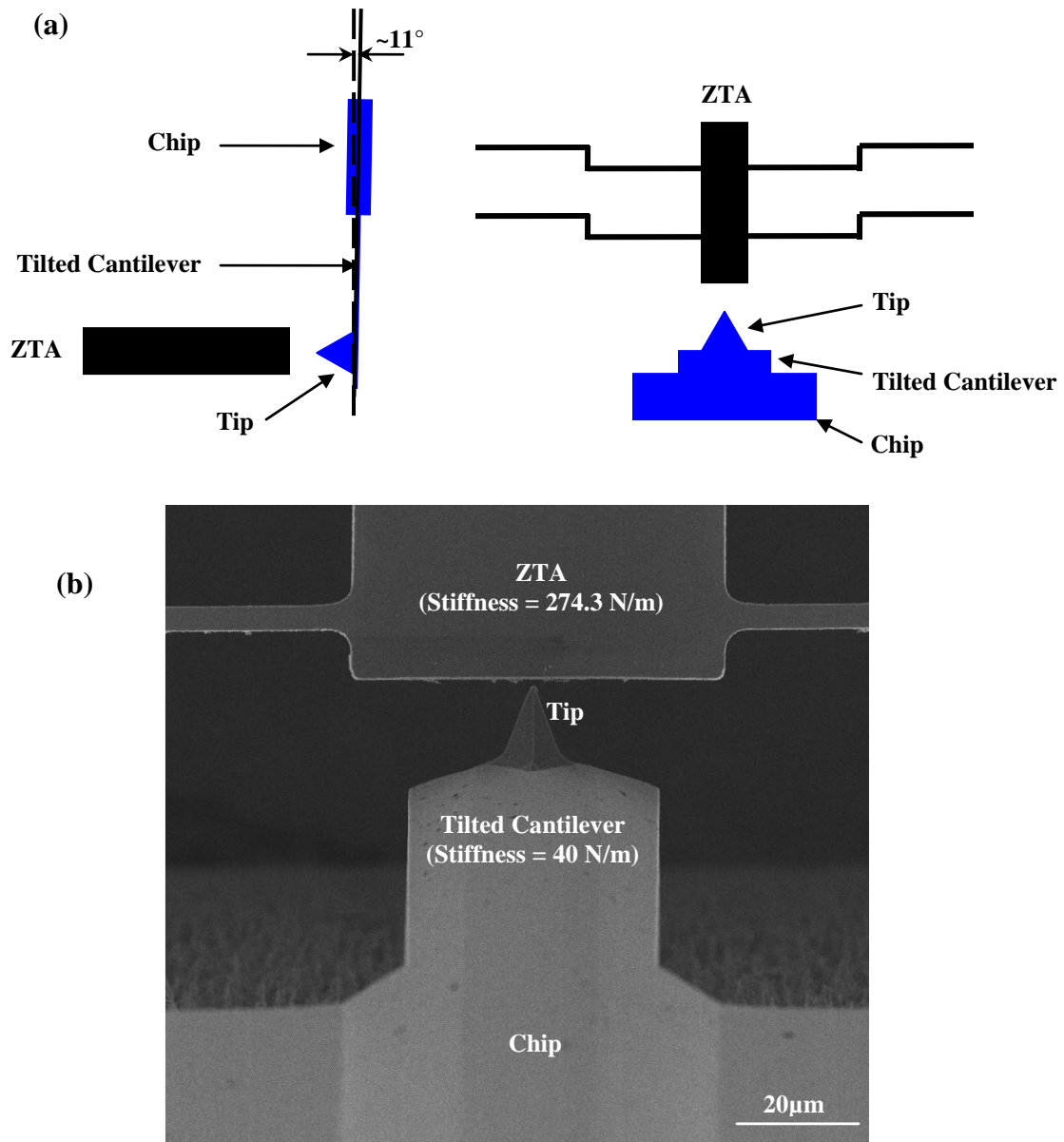


Figure 4.6 Overview of the closed-loop feedback experiment. The AFM cantilever is oriented perpendicular to the ZTA and parallel to the electron beam. The AFM tip is used to push the ZTA. (a) A schematic showing the position of the ZTA and cantilever. Left is side view and right is top view.  $11^\circ$  tilt of the AFM cantilever is used to ensure a clear observation of the setup. (b) SEM image showing the overview of the closed-loop feedback setup.

In the feedback control experiments, the stiffness of the blocking object (applying the external force) cannot be infinite as the tungsten probe used in the piezoresistivity measurements. Consequently, an atomic force microscope (AFM) cantilever (Model ACTA, Nanoscience Instruments) with a stiffness of 40 N/m was used. The AFM cantilever was oriented perpendicular to the ZTA and parallel to the electron beam as shown in Figure 4.6(a). An overview of the experimental setup inside SEM is shown in Figure 4.6(b).

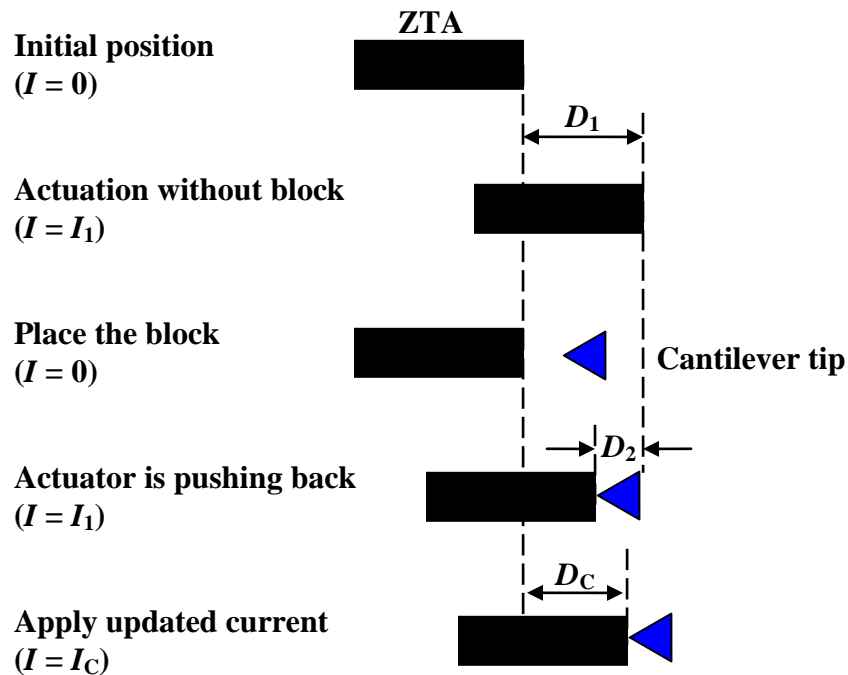


Figure 4.7 The feedback control experiment to maintain a constant position of the ZTA. Ideally  $D_C$  equals  $D_1$ .

The feedback control system experiments were also carried out inside the SEM chamber, with the same experimental conditions as in the piezoresistivity experiments. The experimental process is shown schematically in Figure 4.7. Initially, the process was the same as the piezoresistivity experiment from step 1) to step 4). Then, the output voltage was read into the computer through the input port of the data acquisition module. How much the updated current should be applied to generate the corresponding displacement for counteracting the external force was calculated by the LabVIEW 8.5 program in real time.

Finally, the updated current was written out to the ZTA through the output port of the data acquisition module.

Table 4.1 The comparison of original current and updated current under different external force applied for feedback experiment.

Initial Current (mA)	External Force ( $\mu\text{N}$ )	Updated Current (mA)
8	45.53	8.56
8	99.74	8.94
8.5	75.84	9.03
8.5	109.92	9.17
9	120.281	9.41
9	178.175	9.53
9.3	113.01	9.56
9.3	127.165	9.575
9.3	226.29	9.703
9.5	98.91	9.65
9.5	323.104	9.85
9.5	355.137	9.87

The performance of the feedback control system under different current levels (from 8.0 to 9.5 mA) was tested. Table 4.1 lists all the initial currents, measured external forces (using the feedback system) and the updated currents. The displacements of the ZTA after applying the updated current were compared with the case of no external force (AFM cantilever). The actuator movements were independently measured by SEM images. To evaluate the accuracy of the feedback system, an error coefficient,  $\varepsilon$ , is introduced as follows

$$\varepsilon = \frac{|D_C - D_1|}{D_1 - D_2} \times 100\% \quad (4.5)$$

where  $D_C$  is the displacement of the ZTA after applying the updated current with the presence of the AFM cantilever,  $D_1$  is the displacement of the ZTA without the external

force, and  $D_2$  is the displacement with the external force (as shown in Figure 4.7). The smaller  $\varepsilon$ , the better the feedback accuracy.  $\varepsilon = 0$  means the ZTA is moved back to the initial position.

The distribution of  $\varepsilon$  as a function of the external force at different current levels is plotted in Figure 4.8. It is seen that the error coefficient is smaller than 10% in nearly all cases (except one case), which indicates that the feedback system works quite well. Main error sources include resistance measurement, displacement measurement using SEM and data fitting. Wheatstone Bridge [41;49], is a common method to improve the performance in resistance measurement.

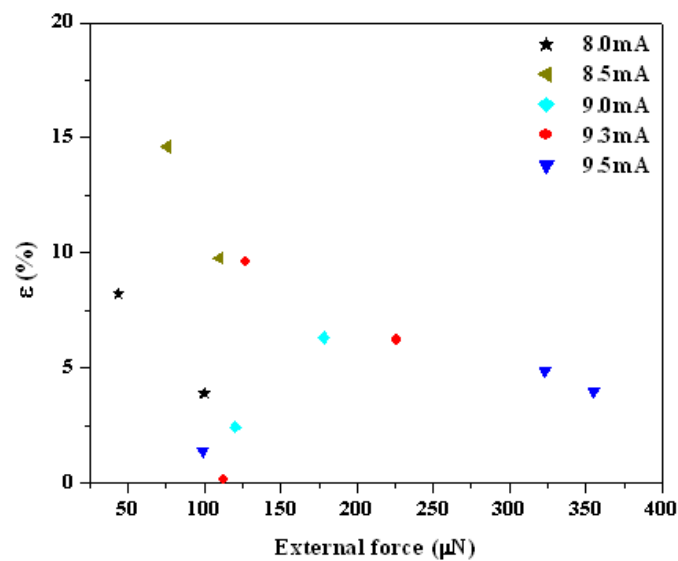


Figure 4.8 The error of the feedback control system.

## Chapter 5 Conclusion

In this project, we firstly described the mechanism of the Z-shaped thermal actuator (ZTA) and theoretically analyzed the displacement, average temperature, stiffness of the structure by energy method. We built a 3-D model depending upon the real geometry and dimensions of the ZTA for multiphysics simulation including electrical, thermal, and mechanical fields. The multiphysics simulation was performed in ANSYS 11.0 with the input of current ranging from 0 to 9.5 mA to mimic the static response of the device under condition of vacuum and room temperature. The displacement, temperature, and voltage distributions were output signals we observed in the simulation. Static response testing was performed under the SEM in vacuum. The relationship among the applied current, actuator deflection and output voltage of the ZTA was measured. After comparing the experimental results with the simulated results, we can verify they are coincident. Dynamic response, such as the time constant and resistance versus frequency, etc. were tested and bode plot was shown in Chapter 2.

Piezoresistive effect of the ZTA was presented in Chapter 3. It was found that the output voltage decrease with the increasing external force pushing the ZTA back. The sensitivity and noise increase with the increasing applied current. In addition, the relationship between two inputs, namely current and external force, and two outputs, namely resistance and actuator deflection, was obtained. Multiphysics simulations, including piezoresistive, electrical, thermal and mechanical fields, were performed in ANSYS 11.0, which provided reasonable agreement with the experimental results.

In Chapter 4, we applied closed-loop to the ZTA to hold its position. The ZTA is treated as a two-input (applied current and external force) and two-output (displacement and electric resistance) system here. Depending upon the calibration between the inputs and outputs, we built the closed-loop in LabVIEW. Different current levels (ranging from 6 to 9.5 mA) with different external force at each current level were tested. It is seen that the error coefficient,  $\varepsilon$ , is smaller than 10% in nearly all cases (except one case), which indicated that

the feedback system works quite well. Closed-loop performance is limited mainly by resistance measurement, displacement measurement using SEM and data fitting.

## 5.1 Future Work

- The static response testing can only test the displacement and resistance of the ZTA with the input. Temperature testing is needed to compare with the simulation results. RAMAN spectroscopy will be used in the future experiment for testing the temperature distribution of the ZTA. Depending upon the relation between the temperature and the spectrum of single crystalline silicon, we will be able to indicate the temperature distribution of the ZTA with different applied current levels.
- The major errors of the feedback control experiments come from unstable environmental condition, fitting equation error and thermal drift. Employing a Wheatstone bridge would be a good method to solve this problem. However, we need 4 devices with the same geometry and dimensions in the same chip. Therefore, a bunch of new devices have been designed for this purpose (Figure A-1).
- PID controller will be integrated into the system to optimize the performance. And all the feedback control experiment will be redone under SEM based upon the new system for more accurate control.
- One application of feedback system is integration of nanomaterial testing system. Once the system is initialized, the position of the ZTA would be fixed. Therefore we could use it to test the relaxation phenomenon (fix the position and test the force generated) of the nanomaterials.

## REFERENCES

- [1] Q.-A.Huang and N.K.S.Lee, "Analysis and Design of Polysilicon Thermal Flexure Actuator," *J. Micromech. and Microeng.*, vol. 9, pp. 64-70, 1999.
- [2] C.Guan and Y.Zhu, "An Electrothermal Microactuator with Z-Shaped Beams," *J. Micromech. and Microeng.*, vol. 20, 085014, (9pp), 2010.
- [3] R.Cragun and L.L.Howell, "Linear Thermomechanical Microactuators," *Proc.1999 ASME International Mechanical Engineering Congress and Exposition, Microelectromechanical Systems (MEMS)*, 1999, pp. 181-188.
- [4] L.Que, J.-S.Park, and Y.B.Gianchandani, "Bent-Beam Electrothermal Actuators-Part I: Single Beam and Cascaded Devices," *J. Microelectromech. Syst.*, vol. 10, no. 2, pp. 247-254, June2001.
- [5] Y.Zhu, A.Corigliano, and H.D.Espinosa, "A Thermal Actuator for Nanoscale in situ Microscopy Testing: Design and Characterization," *J. Micromech. and Microeng.*, vol. 16, pp. 242-253, Feb.2006.
- [6] Y.Zhu and H.D.Espinosa, "An Electromechanical Material Testing System for in situ Electron Microscopy and Applications," *Proc. Nat. Acad. Sci.*, 102, 2005, pp. 14503-14508.
- [7] Y.Zhu, N.Moldovan, and H.D.Espinosa, "A Microelectromechanical Load Sensor for in situ Electron and X-Ray Microscopy Tensile Testing of Nanostructures," *Appl. Phys. Lett.*, vol. 86, no. 1, 013506, (3pp), Jan.2005.
- [8] J.-S.Park, L.L.Chu, A.D.Oliver, and Y.B.Gianchandani, "Bent-Beam Electrothermal Actuators-Part II: Linear and Rotary Microengines," *J. Microelectromech. Syst.*, vol. 10, no. 2, pp. 255-262, Jan.2001.
- [9] L.L.Chu and Y.B.Gianchandani, "A Micromachined 2D Positioner with Electrothermal Actuation and Sub-Nanometer Capacitive Sensing," *J. Micromech. and Microeng.*, vol. 13, no. 2, pp. 279-285, 2003.
- [10] M.S.Baker and L.L.Howell, "On-Chip Actuator of an In-Plan Compliant Bistable Micromechanism," *J. Microelectromech. Syst.*, vol. 11, no. 5, pp. 566-573, Oct.2002.
- [11] W.Tang, T.Nguyen, M Judy, and R.Howe, "Electrostatic-Comb Drive of Lateral Polysilicon Resonators," *Sens. Actuators A, Phys.*, vol. 21, no. 1-3, pp. 328-331, Feb.1990.

- [12] W. Ye, "Optimal Design and Fabrication of Micro-Electro-Mechanical Structures-with Applications to Comb Drives." Ph.D. dissertation Cornell Univ., Ithaca, NY, 1998.
- [13] C.Chen, C.Lee, Y.Lai, and W.Chen, "Development and Application of Lateral Comb-Drive Actuator," *Jpn. J. Appl. Phys.*, vol. 42, pp. 4059-4062, Feb.2003.
- [14] J.Dong, D.Mukhopadhyay, and P.M.Ferreira, "Design, Fabrication and Testing of Silicon-on-Insulator (SOI) MEMS Parallel Kinematics SY Stage," *J. Micromech. and Microeng.*, vol. 17, no. 6, pp. 1154-1161, Jun. 2007.
- [15] C.Liu, *Foundations of MEMS*. Upper Saddle River, NJ: Pearson Prentice Hall, 2006.
- [16] D.Hah, S.Huang, J.Tsai, H.Toshiyoshi, and M.C.Wu, "Low-Voltage, Large-Scan Angle MEMS Analog Micromirror Arrays with Hidden Vertical Comb-Drive Actuators," *J. Microelectromech. Syst.*, vol. 13, no. 2, pp. 279-289, Apr.2004.
- [17] D.Hah, C.A.Choi, C.K.Kim, and D.H.Jun, "A Self-Aligned Vertical Comb-Drive Actuator on a SOI Wafer for a 2D Scanning Micromirror," *J. Micromech. and Microeng.*, vol. 14, pp. 1148-1156, 2004.
- [18] C.Liu and Y.Bar-Cohen, "Scaling Laws of Microactuators and Potential Applications of Electroactive Polymers in MEMS," *Proc.of SPIE's 6th Annual International Symposium on Smart Structures and Materials*, Newport Beach, CA, 1999.
- [19] H.Espinosa, Y.Zhu, and N.Moldovan, "Design and Operation of a MEMS-Based Material Testing System for Nanomechanical Characterization," *J. Microelectromech. Syst.*, vol. 16, no. 5, pp. 1219-1230, Oct.2007.
- [20] E.Enikov and K.Lazarov, "PCB-Integrated Metallic Thermal Microactuators," *Sens. Actuators A, Phys.*, vol. 15, pp. 76-82, June2003.
- [21] N.J.Conway, Z.J.Traina, and S.G.Kim, "A Strain Amplifying Piezoelectric MEMS Actuator," *J. Micromech. and Microeng.*, vol. 17, no. 4, pp. 781-787, Mar.2007.
- [22] J.Z.Tsai, C.J.Chen, W.Y.Chen, J.T.Liu, C.Y.Liao, and Y.M.Hsin, "A New PZT Piezoelectric Sensor for Gravimetric Applications Using The Resonance-Frequency Detection," *Sens. Actuators B*, vol. 139, no. 2, pp. 259-264, June2009.
- [23] C.S.Smith, "Piezoresistance Effect in Germanium and Silicon," *Phys. Rev.*, vol. 94, no. 1, pp. 42-49, 1954.
- [24] M.Tortonese, R.C.Barrett, and C.F.Quate, "Atomic Resolution with an Atomic Force Microscope Using Piezoresistive Detection," *App. Phys. Lett.*, vol. 62, pp. 834-836, 1993.

- [25] B.W.Chui, T.W.Kenny, H.J.Mamim, B.D.Terris, and D.Rugar, "Independent Detection of Vertical and Lateral Forces with a Sidewall-Implanted Dual-Axis Piezoresistive Cantilever," *App. Phys. Lett.*, vol. 72, pp. 1388-1390, 1998.
- [26] J.Brugger, J.Burger, M.Binggeli, R.Imura, and N.F.de Rooij, "Lateral Force Measurements in a Scanning Force Microscope with Piezoresistive Sensors," *Transducers '95.The 8th International Conference on Solid-State Sensors and Actuators, and Eurosensors IX*, 1995, pp. 636-639.
- [27] B.Bae, B.R.Flachsbart, K.Park, and M.A.Shannon, "Design Optimization of a Piezoresistive Pressure Sensor Considering The Output Signal-to-Noise Ratio," *J. Micromech. and Microeng.*, vol. 14, pp. 1597-1607, Dec.2004.
- [28] K.Petersen, J.Brown, T.Vermeulen, P.Barth, J.Mallon, and J.Bryzek, "Ultra-Stable, High-Temperature Pressure Sensors Using Silicon Fusion Bonding," *Sens. Actuators A, Phys.*, vol. 21, no. 1-3, pp. 96-101, Feb.1990.
- [29] E.Peiner, A.Tibrewala, R.Bandorf, S.Biehl, H.Luthje, and L.Doering, "Micro force Sensor with Piezoresistive Amorphous Carbon Strain Gauge," *Sens. Actuators A, Phys.*, vol. 130-131, no. 14, pp. 75-82, Aug.2006.
- [30] N.Yazdi, F.Ayazi, and K.Najafi, "Micromachined Inertial Sensors," *Proc. of The IEEE*, vol. 86, 1998, pp. 1640-1659.
- [31] A.Partridge, J.K.Reynolds, B.W.Chui, E.M.Chow, A.M.Fitzgerald, L.Zhang, N.I.Maluf, and T.W.Kenny, "A High-Performance Planar Piezoresistive Accelerometer," *J. Microelectromech. Syst.*, vol. 9, no. 1, pp. 58-66, Mar.2000.
- [32] B.Lwo and S.Wu, "Calibrate Piezoresistive Stress Sensors Through the Assembles Structure," *J. Electron. Packag.*, vol. 125, no. 2, pp. 289-293, June2003.
- [33] M.C.Hsieh, Y.K.Fang, M.Ju, G.Chen, J.Ho, C.H.Yang, P.M.Wu, G.S.Wu, and T.Y.Chen, "A Contact-Type Piezoresistive Micro-Shear Stress Sensor for Above-Knee Prostresis Application," *J. Microelectromech. Syst.*, vol. 10, no. 1, pp. 121-127, Mar.2001.
- [34] F.Gretillat, M.Gretillat, and N.F.de Rooij, "Improved Design of a Silicon Micromachined Gyroscope with Piezoresistive Detection and Electromagnetic Excitation," *J. Microelectromech. Syst.*, vol. 8, no. 3, pp. 243-250, Sept.1999.
- [35] X.Li, X.Chen, Z.Song, P.Dong, Y.Wang, J.Jiao, and H.Yang, "A Microgyroscope with Piezoresistance for Both High-Performance Coriolis-Effect Detection and Seesaw-Like Vibration Control," *J. Microelectromech. Syst.*, vol. 15, no. 6, pp. 1698-1707, Dec.2006.

- [36] A.Wisitsoraat, V.Patthanasetakul, T.Lomas, and A.Tuantranont, "Low Cost Thin Film Based Piezoresistive MEMS Tactile Sensor," *Sens. Actuators A, Phys.*, vol. 139, no. 1-2, pp. 17-22, Sept.2007.
- [37] A.Tibrewala, A.Phataralaoha, and S.Buttgenbach, "Development, Fabrication and Characterization of a 3D Tactile Sensor," *J. Micromech. and Microeng.*, vol. 19, no. 12, p. 125005 (5pp), Dec.2009.
- [38] D.Li, T.Zhao, Z.Yang, and D.Zhang, "Monolithic Integration of a Micromachines Piezoresistive Flow Sensor," *J. Micromech. and Microeng.*, vol. 20, no. 3, 035024 (8pp), Mar.2010.
- [39] Y.Kanda, "Piezoresistance Effect of Silicon," *Sens. Actuators A, Phys.*, vol. 28, pp. 83-91, 1991.
- [40] W.P.Mason and R.N.Thurston, "Use of Piezoresistive Materials in the Measurement of Displacement, Force, and Torque," *J. Acoust. Soc. Am.*, vol. 29, no. 10, pp. 1096-1101, Oct.1957.
- [41] A.A.Barlian, W.-T.Park, J.Mallon, A.J.Rastegar, and B.L.Pruitt, "Semiconductor Piezoresistance for Microsystems," *Proc. IEEE*, vol. 97, no. 3, pp. 513-552, Mar.2009.
- [42] D.Dadeppo, *Introduction to Sttuctural Mechanics and Analysis*. Upper Saddle River, NJ: Prentice Hall, 1999.
- [43] K.Miller, A.Gowen, G.Hames, and B.Hardy, *SOIMUMPs Design Handbook*. [Online]. Available: <http://www.memscap.com/mumps/documents/SOIMUMPs.dr.v4.pdf>, 2011.
- [44] M.Chiao and L.Lin, "Self-Buckling of Micromachined Beams under Resistive Heating," *J. Microelectromech. Syst.*, vol. 9, no. 1, pp. 146-151, Mar.2000.
- [45] R.Hickey, D.Sameoto, T.Hubbard, and M.Kujath, "Time And Frequency Response of Two-Arm Micromachined Thermal Actuators," *J. Micromech. and Microeng.*, vol. 13, pp. 40-46, Nov.2003.
- [46] T.L.Waterfall, K.B.Teichert, and B.D.Jensen, "Simultaneous On-Chip Sensing and Actuation Using the Thermomechanical In-Plane Microactuator," *J. Microelectromech. Syst.*, vol. 17, no. 5, pp. 1204-1209, Oct.2008.
- [47] G.K.Johns, L.L.Howell, B.D.Jensen, and T.W.McLain, "A Model for Predicting the Piezoresistive Effect in Microflexures Experiencing Bending and Tension Loads," *J. Microelectromech. Syst.*, vol. 17, no. 1, pp. 226-235, Feb.2008.

- [48] O.N.Tufte and E.L.Stelzer, "Piezoresistive Properties of Silicon Diffused Layers," *J. Appl. Phys*, vol. 34, no. 2, pp. 313-318, 1963.
- [49] R.K.Messenger, Q.T.Aten, T.W.McLain, and L.L.Howell, "Piezoresistive Feedback Control of a MEMS Thermal Actuator," *J. Microelectromech. Syst.*, vol. 18, no. 6, pp. 1267-1278, Dec.2009.

**APPENDICES**

## Appendix A

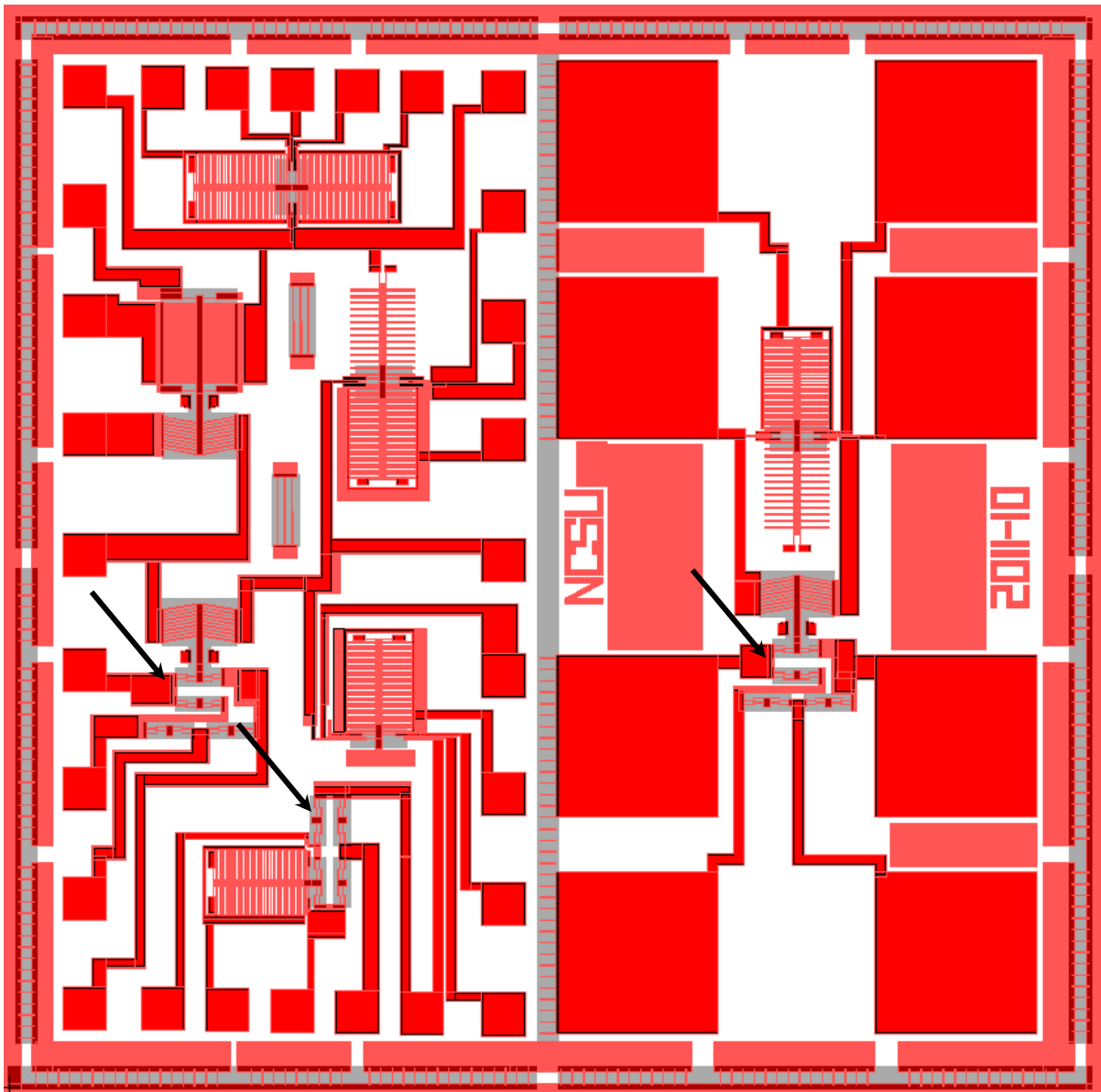


Figure A-1 The layout drawing of SOIMUMPs 10mm × 10mm chip. The arrows show the Wheatstone bridge of Z-shaped thermal actuator.